Simulations of ^{7}Be and ^{10}Be with the GEOS-Chem global model v14.0.2 using state-of-the-art production rates

Minjie Zheng[1,2,3*], Hongyu Liu[4,5], Florian Adolphi[6,7], Raimund Muscheler[2], Zhengyao Lu[8], Mousong Wu[9], and Nønne L. Prisle[3*]

[1]Institute for Atmospheric and Climate Science, ETH Zürich, Zürich, Switzerland
[2]Department of Geology, Lund University, Lund, Sweden
[3]Center for Atmospheric Research, University of Oulu, Oulu, Finland
[4]National Institute of Aerospace, Hampton, Virginia, USA
[5]Science Directorate, NASA Langley Research Center, Hampton, Virginia, USA
[6]Alfred Wegener Institute, Helmholtz Centre for Polar and Marine Research, Bremerhaven, Germany
[7]Faculty of Geosciences, Bremen University, Bremen, Germany
[8]Department of Physical Geography and Ecosystem Science, Lund University, Lund, Sweden
[9]International Institute for Earth System Science, Nanjing University, Nanjing, China

Correspondence to: Minjie Zheng (minjie.zheng@env.ethz.ch) and Nønne L. Prisle (nonne.prisle@oulu.fi)

Abstract

The cosmogenic radionuclides ^{7}Be and ^{10}Be are useful tracers for atmospheric transport studies. Combining ^{7}Be and ^{10}Be measurements with an atmospheric transport model can not only improve our understanding of the radionuclide transport and deposition processes but also provide an evaluation of the transport process in the model. To simulate these aerosol tracers, it is critical to evaluate the influence of radionuclide production uncertainties on simulations. Here we use the GEOS-Chem chemical transport model driven by the MERRA-2 reanalysis to simulate ^{7}Be and ^{10}Be with the state-of-the-art production rate from the CRAC:Be (Cosmic Ray Atmospheric Cascade: Beryllium) model considering realistic spatial geomagnetic cut-off rigidities (denoted as P16spa). We also perform two sensitivity simulations: one with the default production rate in GEOS-Chem based on an empirical approach (denoted as LP67), and the other with the production rate from the CRAC:Be but considering only geomagnetic cut-off rigidities for a geocentric axial dipole (denoted as P16). The model results are comprehensively evaluated with a large number of measurements including surface air concentrations and deposition fluxes. The simulation with the P16spa production can reproduce the absolute values and temporal variability of ^{7}Be and ^{10}Be surface concentrations and deposition fluxes on annual and sub-annual scales, as well as the vertical profiles of air concentrations. The simulation with the LP67 production tends to overestimate the absolute values of ^{7}Be and ^{10}Be concentrations. The P16 simulation suggests less than 10% differences compared to P16spa but a significant positive bias (~18%) in the ^{7}Be deposition fluxes over East Asia. We find that the deposition fluxes are more sensitive to the production in the troposphere and downward transport from the stratosphere. Independent of the production models, surface air concentrations and deposition fluxes from all simulations show similar seasonal variations, suggesting a dominant meteorological influence. The model can also reasonably simulate the stratosphere-troposphere exchange process of ^{7}Be and ^{10}Be by producing stratospheric contribution and ^{10}Be/^{7}Be ratio values that agree with measurements. Finally, we illustrate the importance of including the time-varying solar modulations in the production calculation, which significantly improve the agreement between model results and measurements, especially at mid- and high- latitudes. Reduced

40   uncertainties in the production rates, as demonstrated in this study, improve the utility of ^{7}Be and ^{10}Be as aerosol

41   tracers for evaluating and testing transport and scavenging processes in global models. For future GEOS-Chem

42   simulations of ^{7}Be and ^{10}Be, we recommend using the P16spa (versus default LP67) production rate.

1 Introduction

44   The naturally occurring cosmogenic radionuclide ^{7}Be (half-life of 53.2 days) is monitored worldwide and has

45   been recognized as a useful tracer in atmospheric dynamic studies (Aldahan et al., 2001; Hernández-Ceballos et

46   al., 2016; Terzi et al., 2019; Liu et al., 2016). Especially, ratios of radionuclides concentrations with very different

47   half-lives, such as the ^{10}Be/^{7}Be ratio, have become powerful tools (e.g., Liu et al., 2022b; Raisbeck et al., 1981)

48   to disentangle the influence of transport and deposition since both ^{7}Be and ^{10}Be in the troposphere are mainly

49   removed by wet deposition. In this paper, we aim to improve the utility of ^{7}Be and ^{10}Be as tracers for atmospheric

50   transport by using state-of-the-art production rates in a global 3-D chemical transport model.

51   ^{7}Be and ^{10}Be are produced through interactions between atmospheric atoms (mostly oxygen and nitrogen)

52   and incoming cosmic rays in the atmosphere (Lal and Peters, 1967, referred to as LP67 hereafter; Poluianov et

53   al., 2016, referred to as P16 hereafter). Due to the atmospheric depth-profile of fluxes of primary cosmic rays, the

54   formed secondary particles, and their energy, ^{7}Be and ^{10}Be production rates reach their maxima in the lower

55   stratosphere (Poluianov et al., 2016). About two-thirds of ^{7}Be and ^{10}Be are produced in the stratosphere while the

56   rest is produced in the troposphere (Poluianov et al., 2016; Heikkilä and Smith, 2013; Golubenko et al., 2022).

57   Once produced, ^{7}Be and ^{10}Be rapidly attach to aerosol particles and get transported and deposited with their carrier

58   aerosols by wet and dry depositions (Delaygue et al., 2015; Heikkilä et al., 2013). ^{10}Be has a half-life of 1.39

59   million years (Chmeleff et al., 2010) and its decay is thus negligible compared to its average atmospheric residence

60   time (about 1-2 years) (Heikkilä et al., 2008b). During transport away from the regions of their production, the

61   ^{10}Be/^{7}Be ratio increases because ^{7}Be decays. The ratio ^{10}Be/^{7}Be therefore could indicate the path-integrated age

62   of the air mass. Due to different aerosol residence times in the stratosphere (more than 1 year) and troposphere

63   (~weeks), the ^{10}Be/^{7}Be ratio is higher in the stratosphere than in the troposphere. Hence the ^{10}Be/^{7}Be ratio can be

64   used to detect the stratosphere-troposphere exchange.

65   Many studies have focused on understanding the signals in surface ^{7}Be measurements from worldwide

66   monitoring stations (e.g., Hernandez-Ceballos et al., 2015; Rodriguez-Perulero et al., 2019; Uhlar et al., 2020;

67   Ajtić et al., 2021; Burakowska et al., 2021). Due to the cosmogenic origin of ^{7}Be, surface air ^{7}Be concentrations

68   are found to be connected to the 11-year cycle of solar modulation (Leppänen et al., 2010; Zheng et al., 2021a).

69   In addition, ^{7}Be concentrations in the surface air are affected by different meteorological processes depending on

70   locations, such as stratospheric intrusions (Jordan et al., 2003; Pacini et al., 2015; Yamagata et al., 2019),

71   scavenging by precipitation (Chae and Kim, 2019; Kusmierczyk-Michulec et al., 2015), vertical transport in the

72   troposphere (Aldahan et al., 2001; Ajtic et al., 2018; Zheng et al., 2021a) and large-scale atmospheric circulations

73   (Hernández-Ceballos et al., 2022; Terzi and Kalinowski, 2017).

74   The ability of general circulation models (GCMs, e.g., GISS ModelE, ECHAM5-HAM and EMAC) and

75   chemical transport models (CTMs, e.g., GEOS-Chem and GMI) to capture the main characteristics in ^{7}Be and

76   ^{10}Be transport and deposition has been demonstrated in previous studies (e.g., Heikkilä et al., 2008b; Koch and

77   Rind, 1998; Field et al., 2006; Usoskin et al., 2009; Brattich et al., 2021; Spiegl et al., 2022; Liu et al., 2016;

78   Sukhodolov et al., 2017). For example, Usoskin et al. (2009) found that the influence of the solar proton-induced

79 [7]Be production peak at the surface in early 2005 is small through the comparison of GISS ModelE simulations
80 and surface air measurements. Heikkilä et al. (2009) showed that stratospheric [10]Be contribution is dominant in
81 the global [10]Be deposition by tracing tropospheric and stratospheric [10]Be separately in the aerosol-climate model
82 ECHAM5-HAM. Spiegl et al. (2022) used the EMAC climate model to investigate the transport and deposition
83 process of [10]Be produced by the extreme solar proton event in 774/5 A.D. They suggested that the downward
84 transport of [10]Be from the stratosphere is mainly controlled by the Brewer-Dobson circulation in the stratosphere
85 and cross-tropopause transport. By comparing the measurements with GEOS-Chem simulations over January-
86 March 2003, Brattich et al. (2021) found that increased [7]Be values in surface air samples in Northern Europe in
87 early 2003 were associated with the instability of the Arctic polar vortex. They also showed that, while the model
88 generally simulates well the month-to-month variation in surface [7]Be concentrations, it tends to underestimate the
89 observations (see their Table 2) partly due to the use of the default LP67 production rate for a solar maximum
90 year (1958) in the GEOS-Chem model (Liu et al., 2001). By using the GMI CTM driven with four different
91 meteorological datasets, Liu et al. (2016) showed that the observational constraints for [7]Be and observed [7]Be total
92 deposition fluxes can be used to provide a first-order assessment of cross-tropopause transport in global models.
93 In comparison to GCMs with or without nudged winds (e.g., Golubenko et al., 2021; Heikkilä et al., 2008b; Spiegl
94 et al., 2022) which involve simulating the entire global circulation and climate, the "offline" CTMs are driven by
95 archived meteorological data sets, either from output of GCMs or from atmospheric data assimilation systems.
96 For example, GEOS-Chem can be driven by the GEOS assimilated meteorology (e.g., MERRA-2 reanalysis data;
97 Gelaro et al., 2017a) or output from the GISS GCM (e.g., Murray et al., 2021).

98 In comparison with the LP67 production rate using an empirical approach (Lal and Peters, 1967; Liu et al.,
99 2001; Brattich et al., 2021), the recent production models apply full Monte-Carlo simulations of the cosmic-ray-
100 induced atmospheric nucleonic cascade (e.g., Poluianov et al., 2016; Masarik and Beer, 1999). LP67 shows the
101 highest [7]Be and [10]Be production rates compared to other production models (Elsässer, 2013). P16 suggests that
102 LP67 overestimates the [7]Be production rate by 30-50% compared to their production model (Poluianov et al.,
103 2016). Furthermore, the LP67 production rate implemented in GEOS-Chem is only validated for the year 1958, a
104 year with a high solar modulation function (i.e., high solar activity) of 1200 MeV (Herbst et al., 2017). This
105 highlights the problem of quantitatively comparing these uncorrected model outputs with measurements from
106 other time periods. Some studies (e.g., Koch et al., 1996; Liu et al., 2016) have applied a scale factor to account
107 for this solar modulation influence on LP67 production rate. However, this correction is not ideal as the influence
108 of varying solar modulation is latitudinally and vertically dependent. In earlier studies, the [10]Be production rate in
109 GEOS-Chem was simply scaled to the [7]Be production rate based on the ratio estimated from the surface
110 measurements (Koch and Rind, 1998). In addition, [10]Be as simulated by GEOS-Chem has not been evaluated so
111 far. It is hence necessary to update the [7]Be and [10]Be production rates in GEOS-Chem and assess the corresponding
112 impacts on model simulation results.

113 In this study, we incorporate global [7]Be and [10]Be production rates from the recently published "CRAC:Be"
114 (Cosmic Ray Atmospheric Cascade: Beryllium) model (Poluianov et al., 2016) into the GEOS-Chem model. We
115 simulate [7]Be and [10]Be using GEOS-Chem with the following three production scenarios.

116 • Scenario I: production rate derived from the "CRAC:Be" model considering realistic geomagnetic
117   cut-off rigidity (P16spa production rate)

118   •   Scenario II: production rate derived from the "CRAC:Be" model considering an approximation of

119   geomagnetic cut-off rigidities using a geocentric axial dipole (P16 production rate)

120   •   Scenario III: default production rate in GEOS-Chem using an empirical approximation (LP67

121   production rate)

122   Scenario I is treated as the standard simulation while the other two are sensitivity tests that also enable

123 comparison to earlier studies. This paper is organized as follows. Section 2 introduces the GEOS-Chem model

124 and three different ^{7}Be and ^{10}Be production rates, discusses the methodology and experiment design, and describes

125 the observational data for model evaluations. In section 3, we first investigate the differences between three

126 different production scenarios (section 3.1). Then, we evaluate model simulations of ^{7}Be and ^{10}Be with several

127 published datasets of ^{7}Be and ^{10}Be measurements, in terms of absolute values (section 3.2-3.3), vertical profiles

128 (section 3.4), and seasonal variations (section 3.6). The budgets and residence times of ^{7}Be and ^{10}Be are given in

129 section 3.5. We also examine the ^{10}Be/^{7}Be ratio in the model to assess its ability in capturing the stratosphere-

130 troposphere exchange (section 3.7). Finally, we investigate the influence of including solar-induced production

131 rate variability on ^{7}Be simulations (section 3.8). Summary and conclusions are given in section 4.

132 **2 Models and Data**

133 **2.1 GEOS-Chem model**

134   GEOS-Chem is a global 3-D chemical transport model (http://www.geos-chem.org) that simulates gases and

135 aerosols in both the troposphere and stratosphere (Eastham et al., 2014; Bey et al., 2001). It is driven by archived

136 meteorological data. We use version 14.0.2 (https://wiki.seas.harvard.edu/geos-chem/index.php/GEOS-

137 Chem_14.0.2) to simulate the transport and deposition of atmospheric ^{7}Be and ^{10}Be. We drive the model with the

138 Modern-Era Retrospective analysis for Research and Applications, Version 2 (MERRA-2) meteorological

139 reanalysis (http://gmao.gsfc.nasa.gov/reanalysis/MERRA-2/; Gelaro et al., 2017b). MERRA-2 has a native

140 resolution of 0.5° latitude by 0.667° longitude, with 72 vertical levels up to 0.01 hPa (80 km). Here the MERRA-

141 2 data are re-gridded to 4° latitude by 5° longitude for input to GEOS-Chem for computational efficiency.

142   GEOS-Chem includes a radionuclide simulation option (^{222}Rn-^{210}Pb-^{7}Be-^{10}Be), which simulates transport

143 (advection, convection, boundary layer mixing), deposition, and decay of the radionuclide tracers (e.g., Liu et al.,

144 2001; Liu et al., 2004; Zhang et al., 2021a; Yu et al., 2018) . The model uses the TPCORE algorithm of Lin and

145 Rood (1996) for advection, archived convective mass fluxes to calculate convective transport (Wu et al., 2007),

146 and the non-local scheme implemented by Lin and Mcelroy (2010) for boundary-layer mixing. As mentioned in

147 the introduction section, the standard GEOS-Chem model uses the LP67 ^{7}Be and ^{10}Be production rates. After

148 production, ^{7}Be and ^{10}Be attach to ambient submicron aerosols ubiquitously and their behavior becomes that of

149 aerosols until they are removed by wet deposition (precipitation scavenging) and dry deposition processes. Note

150 that neither is the process of attachment explicitly represented nor is the aerosol size distribution considered in the

151 model. In addition, the decay process is included for the short-lived ^{7}Be with a half-life time of 53.2-day. The

152 decay is minor for the long-living ^{10}Be, which has a half-life time of 1.39 million years (e.g., Chmeleff et al.,

153 2010).

154   Wet deposition includes rainout (in-cloud scavenging) due to stratiform and anvil precipitation (Liu et al.,

155 2001), scavenging in convective updrafts (Mari et al., 2000), and washout (below-cloud scavenging) by

precipitation (Wang et al., 2011). Scavenged aerosols from vertical layers above are allowed to be released to the atmosphere during re-evaporation of precipitation below cloud. In case of partial re-evaporation, we assume that half of the corresponding fraction of the scavenged aerosol mass is released at that level because some of the re-evaporation of precipitation are due to partial shrinking of the raindrops, which does not release aerosol (Liu et al., 2001) . MERRA-2 fields of precipitation formation and evaporation are used directly by the model wet deposition scheme. Dry deposition is based on the resistance-in-series scheme of Wesely (1989). The process of sedimentation is not included in the model.

To quantify the stratospheric contribution to ^{7}Be and ^{10}Be in the troposphere, we separately transport ^{7}Be and ^{10}Be produced in the model layers above the MERRA-2 thermal tropopause (i.e., stratospheric ^{7}Be and ^{10}Be tracers). This approach was previously used to study cross-tropopause transport of ^{7}Be in GEOS-Chem (Liu et al., 2001; Brattich et al., 2021) and Global Modeling Initiative chemical transport models (Liu et al., 2016; Brattich et al., 2017). The stratospheric fractions of ^{7}Be and ^{10}Be are defined as the ratio of the stratospheric ^{7}Be and ^{10}Be concentrations to the ^{7}Be and ^{10}Be concentrations.

2.2 ^{7}Be and ^{10}Be production models

The GEOS-Chem currently uses the LP67 production rates of ^{7}Be and ^{10}Be (Lal and Peters, 1967). These production rates are calculated using an analytically estimated rate of nuclear disintegration (stars) in the atmosphere (stars/g air/s), multiplied by the mean production yield of 0.045 atoms/star for ^{7}Be and 0.025 atoms/star for ^{10}Be (Lal and Peters, 1967). These rates are represented as a function of latitude and altitude for the year 1958 and are not time varying.

Here we update the atmospheric ^{7}Be and ^{10}Be production rates in GEOS-Chem with the latest production model: CRAC:Be model by P16 (Poluianov et al., 2016) using the solar modulation function record by Herbst et al. (2017). The solar modulation function record is based on the local interstellar spectrum by Herbst et al. (2017), which was also used in the production model. Given spatially and temporally resolved geomagnetic cut-off rigidities, the P16 model allows the calculation of 3-dimensional, temporally variable ^{7}Be and ^{10}Be production rates, which are necessary for input to atmospheric transport models. The P16 production model is regarded as the latest and one of the most accurate production models for ^{7}Be and ^{10}Be and was used in recent general circulation model simulations (e.g., Golubenko et al., 2021; Sukhodolov et al., 2017).

The production rates of ^{7}Be and ^{10}Be are calculated by an integral of the yield functions of ^{7}Be and ^{10}Be (Y_i, atoms g^{-1} cm^2 sr), and the energy spectrum of cosmic rays (J_i, (sr sec cm^2)$^{-1}$) above the cutoff energy E_c:

$$Q(\Phi, h, P_c) = \sum_i \int_{E_c}^{\infty} Y_i(E, h) J_i(E, \Phi) \, dE$$

The i refers to different types of primary cosmic ray particles (e.g., proton, alpha and heavier particles). For modelling the contribution of alpha and heavier particles to the total production, their nucleonic ratio in the local interstellar spectrum was set to 0.353 (Koldobskiy et al., 2019). The yield function Y_i is a function of height (h) and kinetic energy per incoming primary nucleon (E) and is directly taken from P16. The energy spectrum of cosmic rays J_i is a function of the kinetic energy (E) and depends on the solar modulation function (Φ)(Herbst et al., 2017). E_c is calculated as a function of the local geomagnetic rigidity cutoff (P_c):

192
$$E_c = E_r\left(\sqrt{1 + \left(\frac{Z_i P_c}{A_i E_r}\right)^2} - 1\right)$$

193   where Z_i and A_i are the charge and mass numbers of particles, respectively. E_r is the rest mass of a proton (0.938
194   GeV).

195   The geomagnetic rigidity cutoff P_c is a quantitative estimation of the Earth's geomagnetic field shielding
196   effect (Smart and Shea, 2005). Cosmic ray particles with rigidity (momentum per unit charge of the particle)
197   higher than the geomagnetic cutoff rigidity value can enter the Earth's atmosphere. In several model simulations
198   of [7]Be and [10]Be (e.g., Field et al., 2006; Koch et al., 1996; Liu et al., 2001), the production is calculated with a P_c
199   simplified as a function of the geomagnetic latitude and geomagnetic dipole moment, called the vertical Stoermer
200   cut-off rigidity equation (see equation 5.8.2-2 in Beer et al., 2012). However, this is different from the real
201   geomagnetic cut-off rigidity inferred from the trajectories of particles with different energies using real
202   geomagnetic field measurements (e.g., Copeland, 2018) which also includes non-dipole moments of the field
203   (Beer et al., 2012) (Fig. S1). Earlier studies suggested that using the simple centered dipole models (e.g., Stoermer
204   cut-off rigidity) for cut-off rigidity approximation is limited as they can significantly distort the cut-off rigidity
205   for some regions (e.g., low-latitude regions) (Pilchowski et al., 2010; Nevalainen et al., 2013)

206   Here we take the geomagnetic cutoff rigidity from Copeland (2018) that provides the cut-off rigidity at a
207   fine interval (one degree) in both latitude and longitude. This production rate is denoted as P16spa. To investigate
208   the effect of this more realistic representation of cut-off rigidity on [7]Be and [10]Be simulations, we also perform
209   simulations where the cut-off rigidities are approximated by the Stoermer equation (denoted as P16). The
210   influence of the geomagnetic field intensity variations can be considered negligible on annual and decadal
211   timescales and are ignored here (e.g. Muscheler et al., 2007; Zheng et al., 2020). It should be mentioned that the
212   LP67 production is based on an ideal axial dipole cut-off rigidity similar to the P16 production model.

213

214   **2.3 GEOS-Chem model experiments and evaluations**

215   An overview of the performed simulations is shown in Table S1. The simulation with the P16spa production rate
216   is considered as the standard simulation while the simulations with the P16 and LP67 production rates are
217   sensitivity tests. The simulation with the P16 production rate is conducted to evaluate the influence of a simplified
218   approximation of cutoff rigidities resulting from a geocentric dipole. In earlier studies, the LP67 production rate
219   was used for global model simulations of [7]Be (e.g., Liu et al., 2016; Brattich et al., 2017; Liu et al., 2001; Koch
220   et al., 1996). The purpose of performing the simulation with the LP67 production rate is to evaluate to what extent
221   model simulations are biased when applying the default LP67 production. Since the LP67 production rate applies
222   only for the year 1958 (with a solar modulation function of about 1200 MeV) and does not consider the influences
223   of the solar variations (e.g., 11-year solar cycle), it underestimates the production rate for the period of 2008-2018
224   that has an average solar modulation function of 500 MeV. To correct for this solar modulation influence, we
225   follow the previous studies (e.g., Liu et al., 2016; Koch et al., 1996) by multiplying the model results by a scale
226   factor of 1.39. It should be noted that this correction is not ideal as the effects of a varying solar modulation on
227   cosmogenic radionuclide production rates depend on altitude and latitude. All simulations are performed from

228   2002 to 2018 with the first six-year for spin-up to make sure the ^{10}Be nearly reaches equilibrium in the atmosphere

229   and the 2008-2018 period (11 years) for analysis. The simulations are conducted using a 4° latitude × 5° longitude

230   resolution for computational efficiency (e.g., Liu et al., 2016; Liu et al., 2004).

231   To evaluate the model's ability to reproduce the variabilities in the observations, we use the statistical

232   parameters: Spearman correlation coefficients and Root Mean Square Error (RMSE) (Chang and Hanna, 2004).

233   Spearman rank correlation (R) (Myers et al., 2013) is used as it does not make any assumptions about the variables

234   being normally distributed. It is less sensitive to outliers in the data compared to the commonly used Pearson

235   correlation. The fraction of modeled concentrations within a factor of 2 of observations (FA2) is calculated, i.e.,

236   for which $0.5 < X_{model}/X_{observation} < 2$. Usually, if the scatter plot of the model and measurements is within a

237   factor of 2 of observations, the model is considered to have a reasonably good performance (e.g., Heikkilä et al.,

238   2008b; Brattich et al., 2021). For model comparison with surface air concentrations, the model value from the

239   bottom grid box closest to the corresponding measurement site is selected.

240

2.4 ^{7}Be and ^{10}Be observational data for model validation

242   The annual mean ^{7}Be surface air concentration and deposition measurements are taken from a compilation by

243   Zhang et al. (2021b). The compilation includes a total of 494 annual mean values for surface air ^{7}Be concentrations

244   and 304 for ^{7}Be deposition fluxes. For the deposition measurements, most of them include both wet and dry

245   deposition, while a few are collected only during rainfall events and thus include only wet deposition. It includes

246   the data from:

- The Environmental Measurements Laboratory (EML, https://www.wipp.energy.gov/namp/emllegacy/index.htm) Surface Air Sampling Program (SASP), which began in the 1980s,

- The ongoing international monitor program Radioactivity Environmental Monitoring (REM) network (e.g., Hernandez-Ceballos et al., 2015; Sangiorgi et al., 2019),

- International Monitoring System (IMS) organized by the Comprehensive Nuclear-Test-Ban Treaty Organization (CTBTO) (e.g., Terzi and Kalinowski, 2017),

- Some additional datasets in publications not included in the above programs.

255   We only include the data covering more than 1 year to reduce the influence of inherent seasonal variations. We

256   further include several recently published data for ^{7}Be surface air concentrations and deposition fluxes records

257   that cover more than 1 year (Burakowska et al., 2021; Liu et al., 2022b; Kong et al., 2022).

258   The dataset used for investigating the seasonality of ^{7}Be surface air concentrations are mainly taken from a

259   multiyear compilation dataset of IMS from Terzi and Kalinowski (2017). The seasonal ^{7}Be deposition data are

260   taken from Courtier et al. (2017), Du et al. (2015), Dueñas et al. (2017), Hu et al. (2020), Lee et al. (2015), and

261   Sangiorgi et al. (2019). The vertical profile of ^{7}Be concentrations is taken from the Environmental Measurements

262   Laboratory (EML) High Altitude Sampling Program (HASP) spanning the years of 1962-1983. It should be noted,

263   different from surface air measurements, the vertical air samples were usually collected during single-day flight

264   campaigns.

265   There are fewer ^{10}Be measurements compared to ^{7}Be. Here we compiled two datasets of published ^{10}Be

266   surface air measurements (Table S2) (Aldahan et al., 2008; Liu et al., 2022a; Yamagata et al., 2019; Padilla et al.,

267 2019; Rodriguez-Perulero et al., 2019; Huang et al., 2010; Méndez-García et al., 2022; Elsässer et al., 2011; Dibb
268 et al., 1994) and deposition fluxes (Table S3) covering more than 1 year, to validate the model performance. The
269 air samples are continuously collected by filters using a high-flow aerosol sampler. The sampling volume is
270 approximately 700 m^3 of air for daily samples (e.g., Liu et al., 2022a) and between 3000 m^3 and 5000 m^3 for
271 weekly samples (e.g., Yamagata et al., 2019). The deposition data include the precipitation samples (wet
272 deposition) (Graham et al., 2003; Monaghan et al., 1986; Somayajulu et al., 1984; Heikkilä et al., 2008a; Raisbeck
273 et al., 1979; Maejima et al., 2005) and ice core samples (wet and dry deposition) that cover the recent period
274 (Heikkilä et al., 2008a; Zheng et al., 2021b; Pedro et al., 2012; Baroni et al., 2011; Aldahan et al., 1998; Berggren
275 et al., 2009; Auer et al., 2009; Zheng et al., 2023b). The ^{10}Be vertical profile measurements are mainly taken from
276 Dibb et al. (1994, 1992) and Jordan et al. (2003).

277

3 Results and Discussions

3.1 ^7Be and ^{10}Be production rates

280 Figure S2 shows the comparison between $^7Be_{P16}$ and $^7Be_{LP67}$ production rates for the year 1958. Generally, the
281 $^7Be_{P16}$ production rate shows a similar production distribution as the $^7Be_{LP67}$ production rate, with a maximum ^7Be
282 production over the polar stratosphere (~100 hPa). The $^7Be_{LP67}$ production rate shows, on average, about 72%
283 higher production rate compared to $^7Be_{P16}$ in the stratosphere and about 38% in the troposphere (Fig. S2c; Table
284 S4). On a global average, the $^7Be_{LP67}$ production rate is about 60% higher than that of $^7Be_{P16}$ as shown in previous
285 studies (Poluianov et al., 2016). The stratospheric production contributes about 67% to the total production for
286 the $^7Be_{LP67}$ production rate while it is about 62% for the $^7Be_{P16}$ production rate for the year 1958.

287   The $^{10}Be_{LP67}$ production rate in the GEOS-Chem model uses the identical source distribution as ^7Be with a
288 scaling factor based on the estimates from surface air measurements (Koch and Rind, 1998). This leads to a
289 constant $^{10}Be_{LP67}/^7Be_{LP67}$ production ratio (0.55) throughout the entire atmosphere. However, as shown in many
290 ^7Be and ^{10}Be production models (e.g., Poluianov et al., 2016; Masarik and Beer, 2009), ^7Be and ^{10}Be have different
291 altitudinal production distributions. The P16 production shows an increasing $^{10}Be/^7Be$ production ratio from
292 higher altitude (0.35) to lower altitude (0.6) (Fig. S3). Using a constant $^{10}Be/^7Be$ production ratio may thus result
293 in large errors in the modeled ^{10}Be concentrations as well as $^{10}Be/^7Be$ ratios. The stratospheric production
294 contributes about 67% of the total production with $^{10}Be_{LP67}$ while it is about 58% with the $^{10}Be_{P16}$ production for
295 the year 1958 (Table S4).

296   Figure 1 shows the comparison between $^7Be_{P16}$ and $^7Be_{P16spa}$ production rates for the period 2008-2018. The
297 global production is similar for P16spa and P16 (Table S4). However, considering non-dipole moment influence
298 on geomagnetic cut-off rigidity, $^7Be_{P16spa}$ and $^{10}Be_{P16spa}$ production rates in the Southern Hemisphere show ~11%
299 higher production rates compared to the Northern Hemisphere (Table S4). This difference is not present when an
300 axial dipole is assumed. Compared to P16 production rate, the $^7Be_{P16spa}$ production rate shows 30-40% lower
301 production over eastern Asia and southeastern Pacific, but 40-50% higher over North America and from
302 subtropical South Atlantic to Australia (Fig. 1). $^{10}Be_{P16spa}$ shows similar results as the $^7Be_{P16spa}$. These differences
303 are not constant throughout the atmospheric column but generally increase with altitude (Fig. 1d).

304

305

306
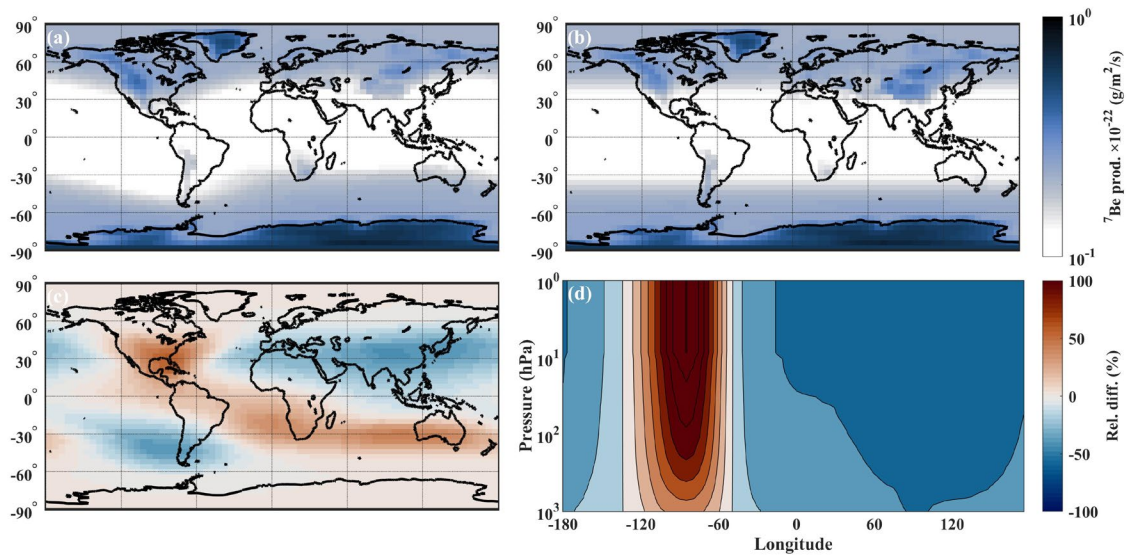
Figure 1. Upper panels: Spatial distribution of (a)^{7}Be$_{P16spa}$ and (b)^{7}Be$_{P16}$ production rates at 825 hPa over the period 2008-2018. Lower panels: (c) Relative differences (%), i.e., (^{7}Be$_{P16spa}$-^{7}Be$_{P16}$)/ ^{7}Be$_{P16}$ ×100%, between production rates with and without considering the detailed spatial cut-off rigidity. (d) Relative differences (%) of the zonal mean production rates between P16spa and P16 at 30°N.

311

3.2 ^{7}Be surface air concentrations and deposition fluxes

Figure 2 compares the simulated ^{7}Be$_{P16spa}$ averaged over 2008-2018 with the measurements. Due to the data availability, the measurements do not necessarily cover the same period as model simulations. The model deposition fluxes here include both dry and wet deposition. About 93.7% of modeled air ^{7}Be$_{P16spa}$ concentrations agree within a factor of 2 with the observed values. The model also shows reasonable agreement with the measured deposition fluxes (60.9% within a factor of 2) although the discrepancy between the modeled and observed deposition fluxes is larger than that for surface air concentrations. The deposition fluxes are usually less well monitored compared to the air ^{7}Be samples and cover usually only shorter periods (e.g., one or two years). Further, the limited model resolution applied here may not be able to capture meteorological conditions on local scales (e.g., precipitation, convection, and tropopause folding) in some sites (e.g., Yu et al., 2018; Spiegl et al., 2022), especially for coastal regions when the sub-grid scale orographic precipitation is important.

323

324
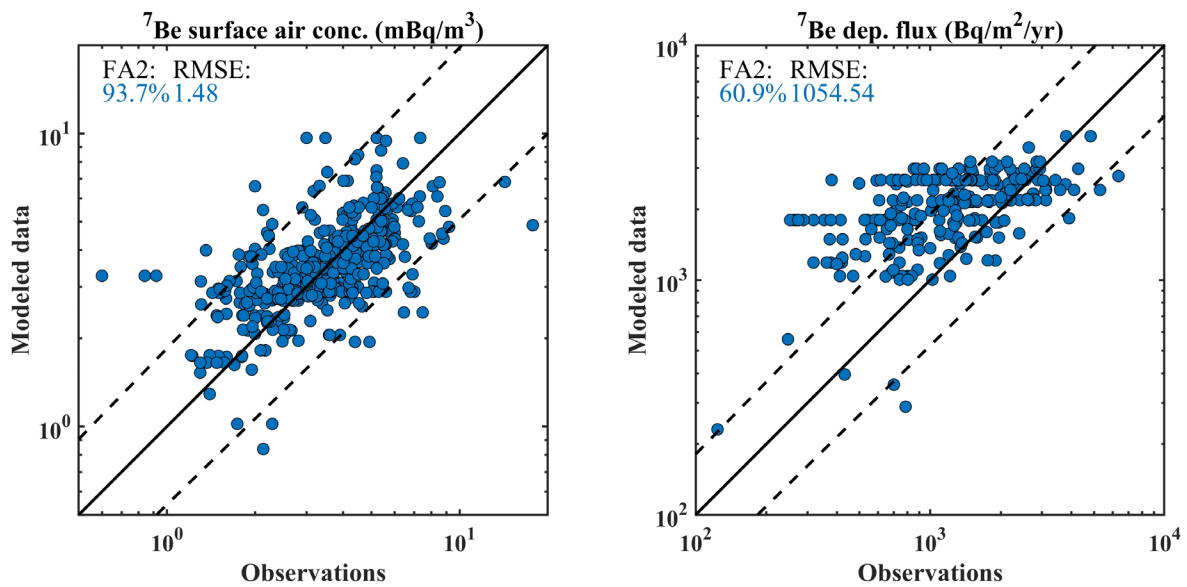
Figure 2. Scatter plot of modeled $^7Be_{P16spa}$ versus observed ^7Be surface air concentrations (left panel) and deposition fluxes (right panel). The model values are averaged over the years of 2008-2018. The dashed lines are the factor of 2 of 1:1 line (straight lines). The "FA2" indicates the fraction of modeled concentrations within a factor of 2 of observations while "RMSE" indicates the root mean square error.

Figure 3 shows the spatial distribution and zonal mean of measurements in comparison with the model simulated $^7Be_{P16spa}$ surface air concentrations and deposition fluxes. Generally, the model captures the spatial distribution of ^7Be air concentrations and deposition fluxes. The "latitudinal pattern" of surface air ^7Be concentrations differs from that of ^7Be production rate, reflecting the effects of atmospheric transport and deposition processes. The model suggests high ^7Be air concentrations mainly over the dry regions (Fig. 3a) due to low wet deposition rates (e.g., desert regions over Northern Africa, Arabian Peninsula, central Australia, and central Antarctica) and over high-altitude regions (e.g., Tibetan Plateau). The model captures the observed latitudinal peaks in surface air concentrations over the subtropics and mid-latitudes (Fig. 3c around 30°N-40°N and 30°S -40°S). These peaks are consistent with the high stratospheric contribution (25%-30%) at mid-latitudes (Fig. S4). The model overestimates ^7Be air concentrations over the Arctic (70°N-90°N, Fig. 3c) by about 30%-40%. By contrast, high ^7Be deposition fluxes are observed at mid-latitudes due to the influence of the high precipitation (wet deposition) and strong stratosphere-troposphere exchange (Fig. 3d). In the Northern Hemisphere, the model simulated deposition fluxes peak at a lower latitude (~30°N) relative to the observations (~45°N). These modeled spatial distributions of the air concentrations and deposition rates of ^7Be also agree generally well with previous model simulations (e.g., Heikkilä and Smith, 2012).

344
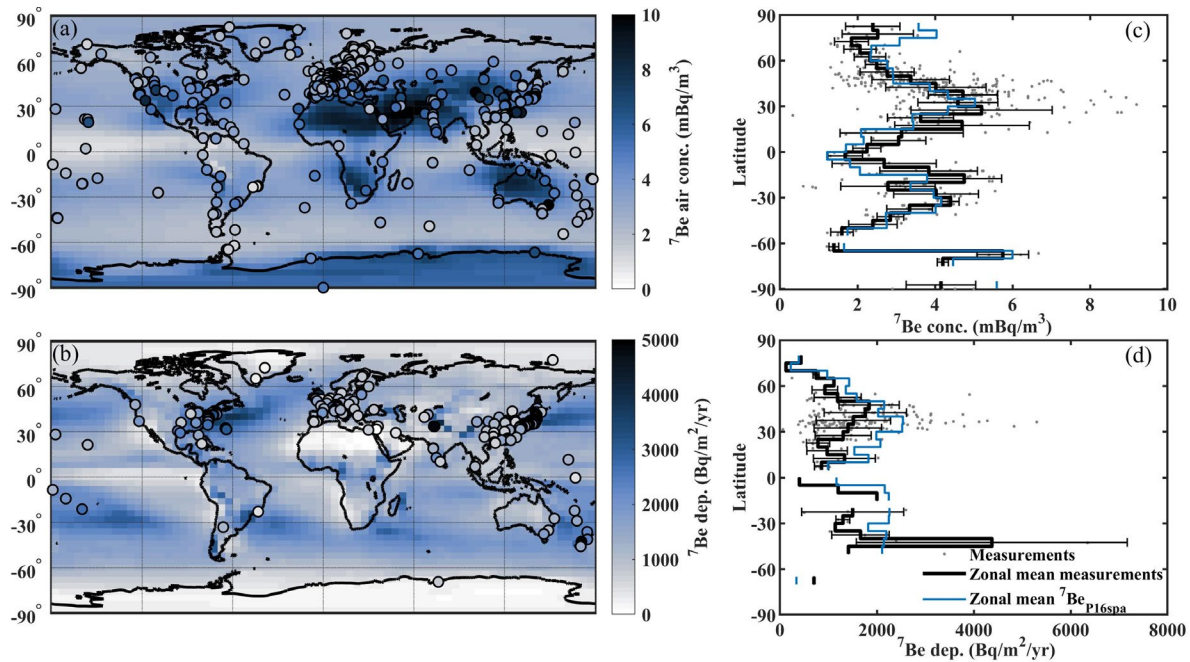
Figure 3. Left column: (a) modeled $^7Be_{P16spa}$ surface air concentrations (mBq/m³) and (b) deposition fluxes (Bq/m²/yr) averaged over the period 2008-2018. Color-coded dots denote ^7Be measurements. Right column: zonal mean of (c) observed ^7Be surface air concentrations and (d) deposition fluxes (black lines, for each 5° latitude bin) compared with the model simulation using the P16spa production rate (blue lines). Dots are individual measurements. The error bars indicate one standard deviation. The outliers, defined as more than three scaled median absolute deviations (MAD) away from the median, are excluded from the calculation. The observations are averaged over the years available.

The modeled $^7Be_{P16spa}$ air concentrations show better agreements (smaller RMSE and higher FA2 values) with the measurements in comparison to $^7Be_{LP67}$ (Fig. S5). $^7Be_{LP67}$ tends to overestimate the absolute values of ^7Be concentrations. This is caused by i) the overestimation of ^7Be production rate by LP67 for a given solar modulation function and ii) using a simple scale factor to account for the solar modulation influence on the LP67 ^7Be production rate.

We also examine whether using the dipole-approximation of the cut-off rigidity or real cut-off rigidity (P16 and P16spa, respectively) in the production model leads to significantly different results (Fig. 4). Although large regional differences (up to 40-50%, Fig. 1) in the production model are observed between P16spa and P16 production rates, such differences are reduced in surface air concentrations and deposition fluxes due to transport and deposition processes, as expected. The $^7Be_{P16sap}$ air concentrations show higher values (~7%) over 10°S-40°S and lower values (~12%) over the east Asian region (Fig. 4) compared to $^7Be_{P16}$. These differences are higher for the deposition fluxes with up to 10% higher over the 10°S-40°S and up to 18% lower over the east Asian region (Fig. 4). Since the total deposition flux reflects precipitation scavenging through the tropospheric column, it tends to be more sensitive to ^7Be air concentrations at higher altitudes and downward transport of ^7Be from the stratosphere. Indeed, model results suggest that deposition fluxes have a higher stratospheric fraction compared to surface air concentrations (Fig. S4), as previously shown by Liu et al. (2016). The $^7Be_{P16spa}$ deposition fluxes show better agreement with measurements than those of $^7Be_{P16}$ (Fig. S5). The comparison for ^{10}Be shows similar results as ^7Be except with less than 10% differences. For ^{10}Be deposition fluxes in Antarctica and Greenland, this influence is less than 3%. This is because the dominant contribution of ^{10}Be is from the stratosphere where the hemispheric production differences are diminished by the long stratospheric residence time of ^{10}Be. However, it does not suggest that the cut-off rigidity including the non-dipole influence could be ignored for ^{10}Be depositions in polar regions, as the spatial pattern of cut-off rigidities was very different in the past time, e.g., during the

374 Laschamps geomagnetic field minimum around 41,000 years before the present (Gao et al., 2022). Further studies

375 are warranted to investigate this spatial cut-off rigidity influence on ^{10}Be in more detail.

376
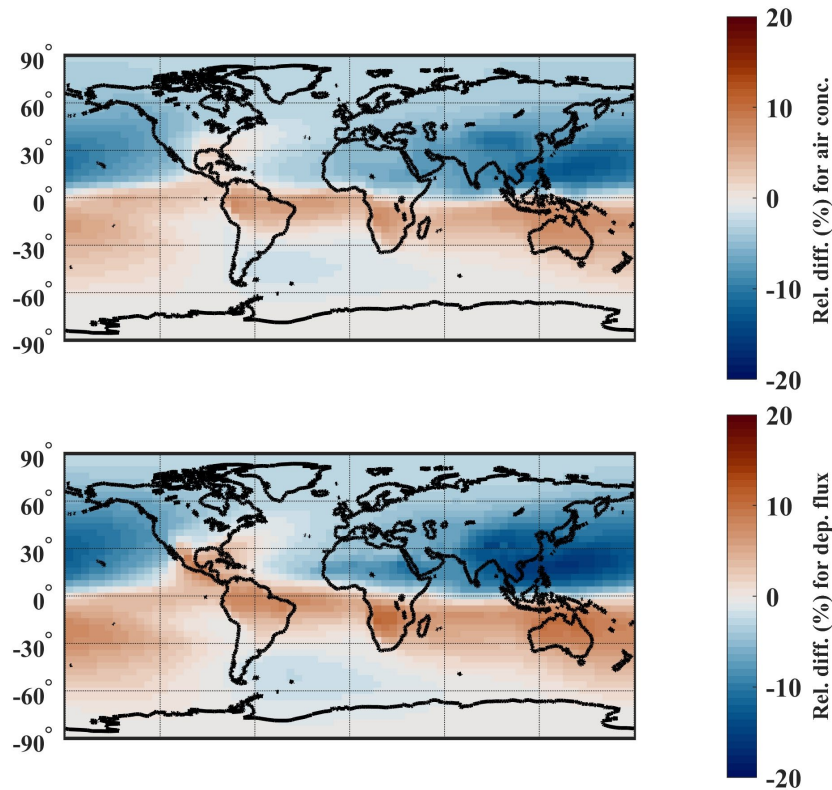
377 **Figure 4**. Relative differences (percentage) of surface air concentrations (upper panel) and deposition fluxes

378 (lower panel) between ^{7}Be$_{P16spa}$ and ^{7}Be$_{P16}$ for the period 2008-2018, i.e., (^{7}Be$_{P16spa}$-^{7}Be$_{P16}$)/^{7}Be$_{P16}$ ×100%.

379

380 **3.3 ^{10}Be surface air concentrations and deposition fluxes**

381 Figure 5 shows the comparison between modeled annual mean ^{10}Be$_{P16spa}$ surface air concentrations (or deposition

382 fluxes) averaged over 2008-2018 and measurements. The ^{10}Be$_{P16spa}$ shows similar spatial distributions as ^{7}Be$_{P16spa}$

383 because both radionuclides share the same transport and deposition processes. The model underestimates the

384 measured ^{10}Be surface air concentrations and deposition fluxes at some sites (Fig. 5b, 5d). This may be attributed

385 to the influence of resuspended dust with ^{10}Be attached, which could typically contribute 10%-35% to the air ^{10}Be

386 concentrations (Monaghan et al., 1986). It should be mentioned that ^{7}Be decays in the dust because of its short

387 half-life, and therefore does not contribute to the surface air ^{7}Be concentrations. Indeed, data where a careful

388 examination of the recycled dust ^{10}Be in samples was conducted (e.g., Monaghan et al., 1986), or from locations

389 that are less influenced by recycled dust ^{10}Be (e.g., Polar regions; dots in Fig. 5b-5d), show better agreement with

390 the model simulations. This suggests the importance of considering the dust contribution when measuring the air

391 ^{10}Be samples. The model also shows relatively good agreement with most ^{10}Be deposition data from polar ice

392 cores (marked as dots in Fig. 5d) within a factor of 2.

393
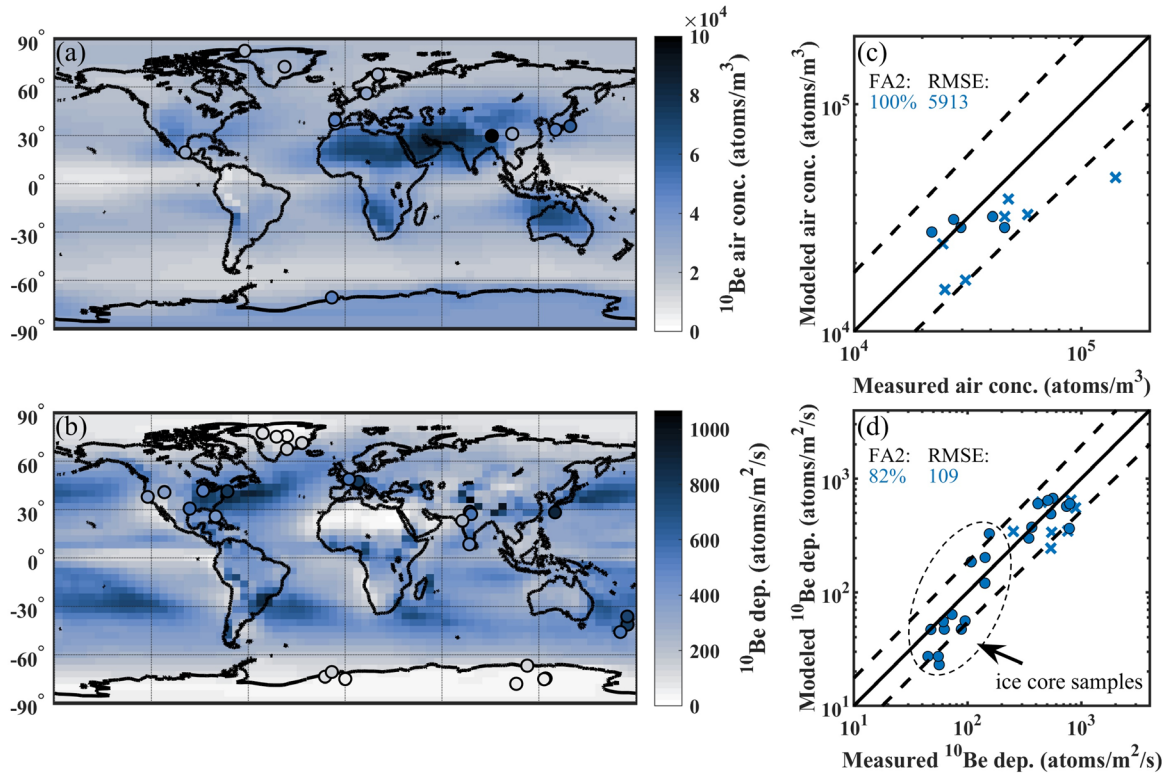
Figure 5. Left column: the modeled annual mean $^{10}Be_{P16spa}$ (a) surface air concentrations and (b) deposition fluxes averaged over 2008-2018 overplotted with measurements (color-coded dots). Right column: (c)-(d) the scatter plot between model results and measurements for (c) surface air concentrations and (d) deposition fluxes. The dots in (c-d) indicate measurements with careful examination of dust ^{10}Be contributions or from the polar regions which are not influenced by dust ^{10}Be. The crosses indicate the samples without examining dust contributions. The FA2 and RMSE are calculated only using the dust-free samples (dots). Blue and orange colors indicate the results using P16spa and LP67 production rates, respectively.

3.4 Vertical profiles of ^{7}Be and ^{10}Be

Figure 6 shows the simulated annual zonal mean vertical profiles of $^{7}Be_{P16spa}$ and $^{10}Be_{P16spa}$ concentrations compared with those from aircraft measurements in the troposphere and stratosphere from the EML/HASP. The measurements cover different regions and specific meteorological conditions; hence they should only provide a range in which the model results should lie. Following previous modelling studies (Heikkilä et al., 2008b; Koch et al., 1996), we compare model zonal mean values in each 15° latitude band with the corresponding observations.

The simulated $^{7}Be_{P16spa}$ profiles agree well with the measurements, especially capturing the peaks at ~20-22 km at mid- and low- latitudes (e.g., Fig. 6c, 6e, 6h). The feature that ^{7}Be increases with altitude without a peak at 22 km at northern high latitudes (60°N-75°N) is also captured by the model (Fig. 6a). The $^{7}Be_{P16spa}$ shows high concentrations in the polar stratosphere and low values over the equatorial stratosphere (Fig. S6), mainly reflecting the latitudinal distribution of the production. This "latitudinal structure" is modulated for $^{10}Be_{P16spa}$ in the stratosphere as ^{10}Be is better mixed than ^{7}Be due to its slow decay together with relatively long residence time in the stratosphere (Waugh and Hall, 2002). Both ^{7}Be and ^{10}Be show very low concentrations in the tropical upper

troposphere, reflecting the frequent injection of air from the lower troposphere in wet convective updrafts, where
aerosols are efficiently scavenged (Fig. S6).
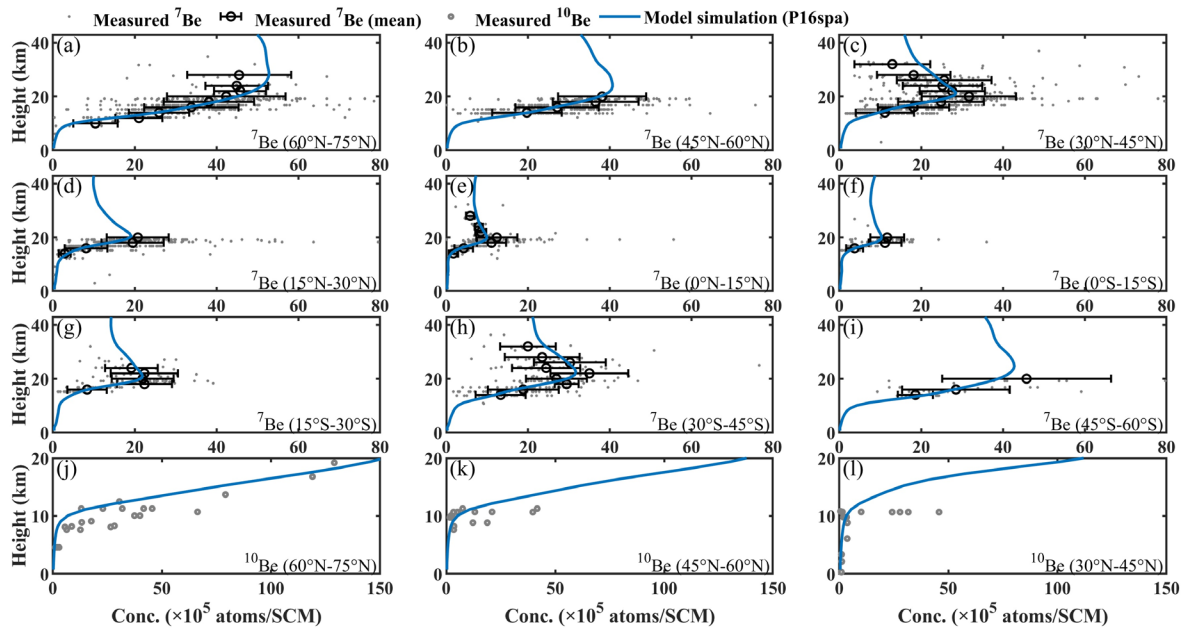
Figure 6. Comparison of the vertical profile between measurements (circles) and model zonal mean $^7Be_{p16spa}$ and $^{10}Be_{p16spa}$ concentrations for each latitudinal band (15°) over the period 2008-2018. The ^7Be (circle with error bar) observations (from the EML/HASP) are averaged for the altitude band of every 2 km where more than 5 samples are available. We exclude the outlier from the calculation, which is defined as more than three scaled median absolute deviations (MAD) away from the median. The ^{10}Be profile measurements are mainly taken from Dibb et al. (1994, 1992) and Jordan et al. (2003).

The model also reasonably simulated ^{10}Be vertical profiles compared with observations, with a tendency to underestimate observations in the stratosphere (Fig. 6j-6l). A previous general circulation model study by Heikkilä et al. (2008b) also showed too low model stratospheric ^{10}Be compared to measurements. They attributed this underestimation to too short stratospheric air residence time in the model, which prevents ^{10}Be concentrations from sufficiently accumulating in the stratosphere. However, this may not be the case in our study, as the stratospheric air residence time in the MERRA-2 reanalysis agrees reasonably with the observations (Chabrillat et al., 2018). Another explanation is that the ^{10}Be production rate may be underestimated in the stratosphere. ^7Be is less affected by this process than ^{10}Be because of its short half-life compared to its stratospheric residence time (Delaygue et al., 2015).

3.5 Global budgets and residence time

Table 1 shows the global budgets for $^7Be_{P16spa}$ and $^{10}Be_{P16spa}$ over the period of 2008-2018. About 22.1% of tropospheric $^7Be_{P16spa}$ is lost by radioactive decay, 75.8% by convective and large-scale precipitation, and 2.1% by dry deposition. The wet deposition contributes to about 97% of total deposition for $^7Be_{P16spa}$ and $^{10}Be_{P16spa}$ (Table 1; Fig. S7), which is slightly higher than the ~93% contribution in previous model studies (Heikkilä et al., 2008b; Koch et al., 1996; Spiegl et al., 2022). The global mean tropospheric residence time of $^7Be_{P16spa}$ is about 21 days, which is comparable to those reported by previous model studies: 18 days by Heikkilä et al. (2008b) and

442 21 days by Koch et al. (1996) and Liu et al. (2001). This also agrees with the residence time of about 22-35 days

443 estimated from the observed deposition fluxes and air concentrations at 30°N - 75°N (Bleichrodt, 1978). The

444 averaged tropospheric residence time of ^{10}Be$_{P16spa}$ is about 24 days, which is consistent with the 20 days suggested

445 by Heikkilä et al. (2008b).

446

447 **Table 1**. Global budgets of ^{7}Be and ^{10}Be averaged over the period 2008-2018 in GEOS-Chem using P16spa.

	^{7}Be$_{P16spa}$	^{10}Be$_{P16spa}$
Sources (g d-1)	0.403	0.256
Stratosphere	0.272 (67.5%)	0.161 (62.9%)
Troposphere	0.131 (32.5%)	0.095 (37.1%)
Sinks (g d-1)	0.404	0.253
Dry deposition	0.004 (1.0%)	0.006 (2.4%)
Wet deposition	0.151 (37.4%)	0.247 (97.6%)
Radioactive decay	0.249 (61.6%)	---
Stratosphere	0.205 (50.7%)	---
Troposphere	0.044 (10.9%)	---
Burden (g)	19.145	89.902
Stratosphere	15.778 (82.4%)	83.785 (93.2%)
Troposphere	3.367 (17.6%)	6.117 (6.8%)
Tropospheric residence time (days)*	21.72	24.08

*Against deposition only

448

3.6 Seasonality in ^{7}Be and ^{10}Be

450 The seasonality of ^{7}Be is influenced by a) the amount of precipitation; b) the stratosphere-troposphere exchange

451 processes; and c) the vertical transport of ^{7}Be in the troposphere. The roles of these factors may vary depending

452 on location. We compare the seasonal variations of modeled ^{7}Be$_{P16spa}$ and ^{7}Be$_{LP67}$ concentrations with

453 measurements from a dataset compiled by Terzi and Kalinowski (2017) with the data covering more than 6 years

454 (Fig. 7). It should be noted that the model ^{7}Be results and MERRA-2 precipitation rates are averaged over the

455 years of 2008-2018 while the measurements are based on the data availability over the period 2001-2015.
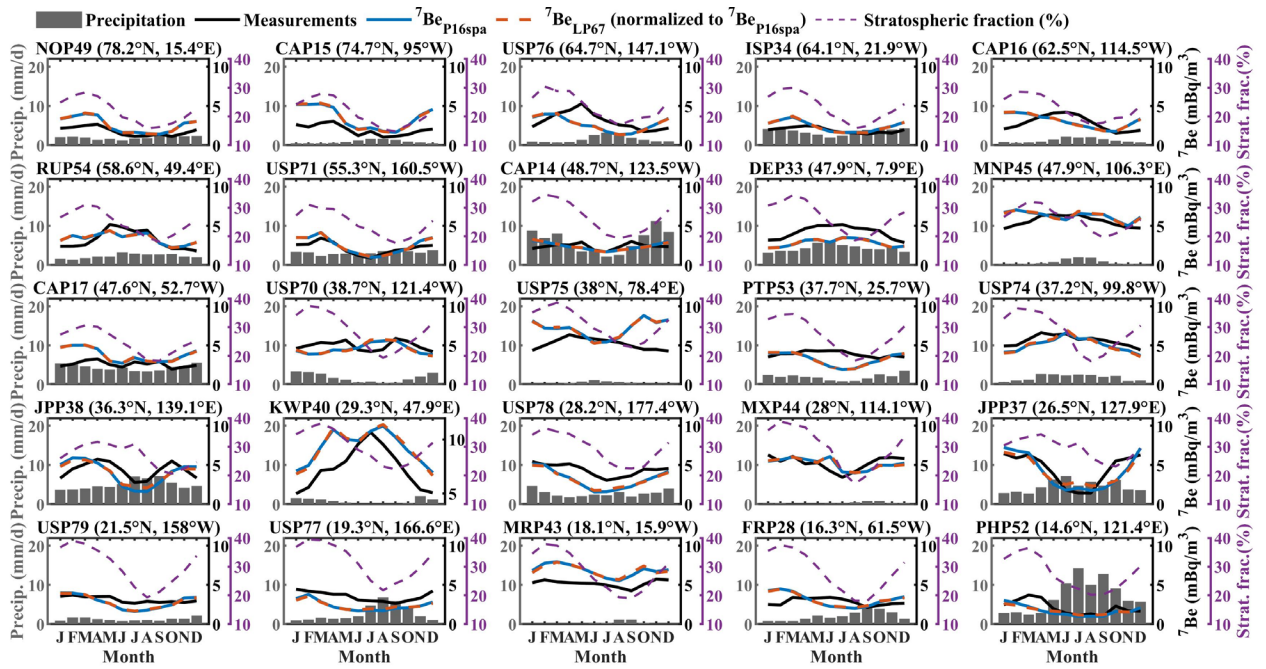
Figure 7. Seasonal cycle of simulated and measured surface air ^7Be concentrations, MERRA-2 total precipitation (4° × 5°, bar graph), and modeled stratospheric contributions to surface air. The plots are arranged based on the site latitudes. The model results using the LP67 production rate are normalized to the ones using the P16spa production rate.
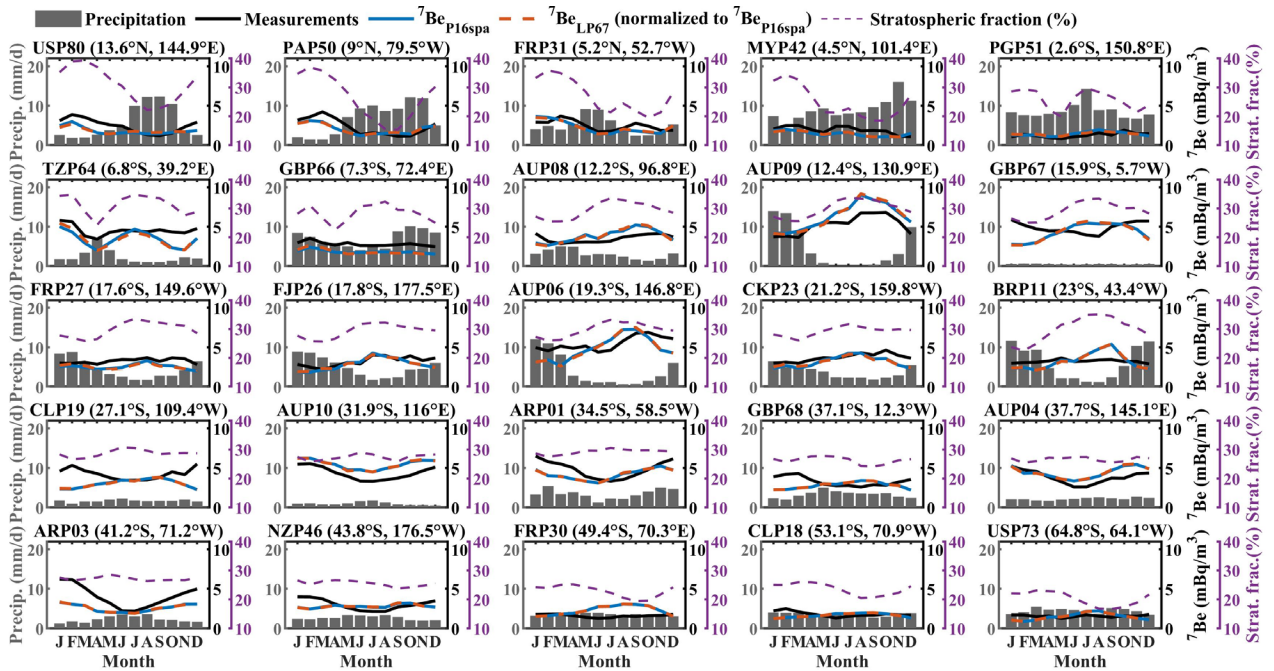
Figure 7. (continued)

In the Southern Hemisphere from 25°S-40°S, the ^7Be concentration peak is observed in austral summer (December-February), resulting from the combined influence of stratospheric intrusions and strong vertical transport during this season (Villarreal et al., 2022; Zheng et al., 2021a; Koch et al., 1996). The summer peak is also observed at northern mid-latitudes. This "summer peak" feature is well simulated by the model at some sites (e.g., KWP40 (29.3°N, 47.9°E), AUP04 (37.7°S, 145.1°E) and AUP10 (31.9°S, 116°E) shown in Fig. 7) but not

467   at others (e.g., GBP68 (37.1°S, 12.3°W) and PTP53 (37.7°N, 25.7°W) in Fig. 7). This may not be related to

468   stratospheric intrusion in the model as the simulated stratospheric contributions (Fig. S4) agree fairly well with

469   estimates inferred from measurements, i.e., ~25% on annual average at northern mid-latitude surface (Dutkiewicz

470   and Husain, 1985; Liu et al., 2016). Hence this could be due to the errors in vertical transport (e.g., convection)

471   during the summer season.

472   The sites at northern high-latitudes (>50°N) show spring peaks that are well simulated by the model (e.g.,

473   ISP3 (64.1°N, 21.9°W)). This spring peak coincides with high stratospheric contributions, reflecting the influence

474   of stratospheric intrusions. The influence of precipitation changes is also seen at several sites, especially in

475   locations with high precipitation rates (e.g., monsoon regions). For example, two sites from Japan (JPP38 (36.3°N,

476   139.1°E) and JPP37 (26.5°N, 127.9°E) in Fig. 7) show summer minima coinciding with the high precipitation,

477   even with relatively high stratospheric contributions in the same month.

478   The seasonal variation of stratospheric contribution is quite similar for the sites located in the Northern

479   Hemisphere, with a high contribution in spring and a low contribution in fall. This is consistent with the estimates

480   based on air samples that indicate stratospheric contributions varying from ~40% in spring to ~15% in fall at

481   latitudes 38°N-51°N (Dutkiewicz and Husain, 1985).

482   Generally, the model simulates well the annual cycle of surface air ^{7}Be concentrations for most sites in terms

483   of amplitude and seasonality (Fig.7). For a few sites (e.g., DEP33 (47.9°N, 7.9°E)), the model captures the

484   observed seasonality but not the correct absolute values. This could be partly due to the coarse resolution of the

485   model. The ^{7}Be$_{LP67}$ is normalized to ^{7}Be$_{P16spa}$ as we focus on the comparison of seasonal variability between these

486   simulations. The very similar features (differences within 1%) between all simulations using different production

487   rates indicate a dominant influence of the meteorological conditions on the seasonal variations of the air ^{7}Be

488   concentrations.

489
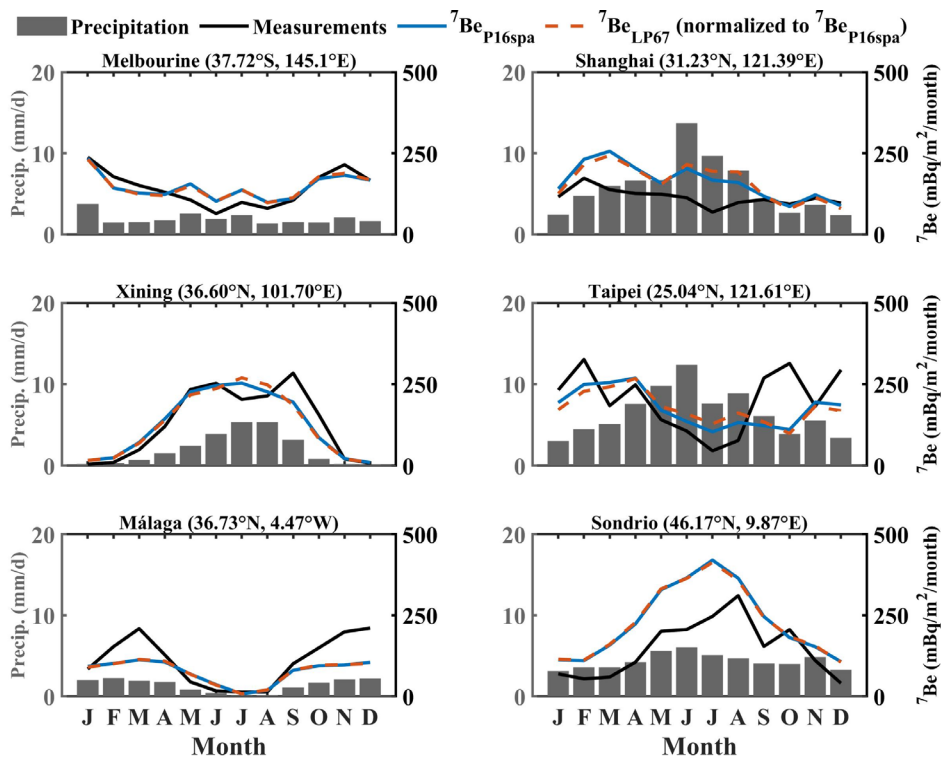
 Figure 8. Seasonal cycle of simulated (color lines) and measured (black line) [7]Be deposition fluxes together with MERRA-2
491 total precipitation (4° × 5°, bar graph). The model results using the LP67 production rate are normalized to the ones using the
492 P16spa production rate.

493   Figure 8 compares model results with the seasonal [7]Be deposition flux observations over the overlapping

494 periods. Usually, high precipitation leads to high [7]Be deposition fluxes (e.g., Du et al., 2015). Interestingly, low

495 deposition fluxes are observed during the summer season in Taipei (Lee et al., 2015; Huh et al., 2006) coinciding

496 with high precipitation. This feature is well-captured in the model. Taipei has a typhoon season in summer when

497 strong precipitation can occur in a very short period. The atmospheric [7]Be could be removed quickly at the early

498 stage of the precipitation event while at the later stage there is little [7]Be left in the air that can be removed

499 (Ioannidou and Papastefanou, 2006).

500   To examine the ability of model to simulate [10]Be in polar regions, we compare model results with two sub-

501 annual ice cores records (Fig. 9): the GRIP record from Greenland (1986-1990) (Heikkilä et al., 2008c) and the

502 DSS record from Antarctica (2000-2009) (Pedro et al., 2011a). It should be noted that the direct measurements

503 from ice cores are concentrations in the ice (atoms/g). To calculate deposition fluxes, the ice concentrations are

504 multiplied with ice accumulation rates. However, for sub-annual accumulations, this bears large uncertainties.

505 Therefore, we calculate the modeled [10]Be concentrations for the selected sites using the model deposition fluxes

506 at the selected sites timed by ice density and then divided by the corresponding model precipitation rates.

507
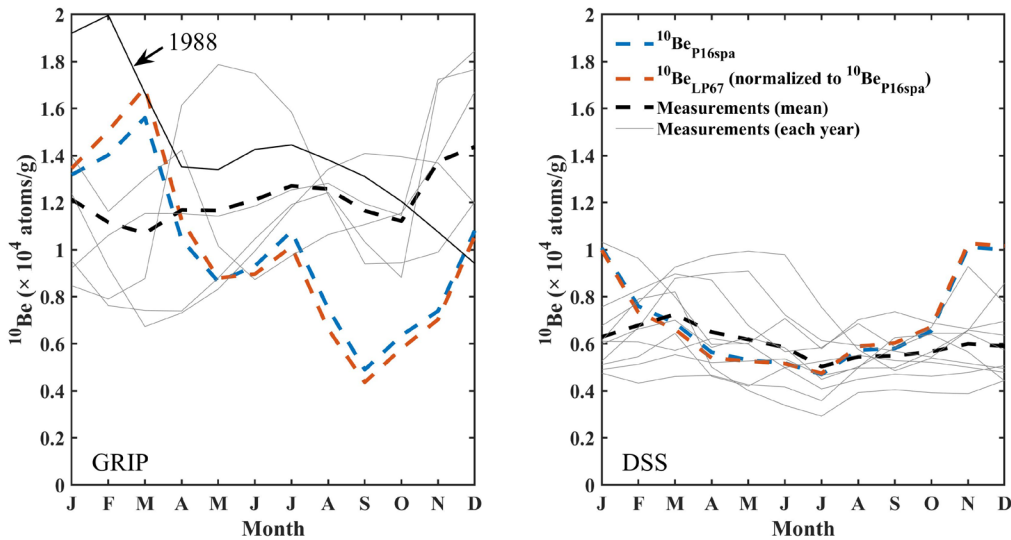
508 **Figure 9**. Seasonal cycle of simulated [10]Be deposition fluxes (2008-2018) and measured [10]Be deposition fluxes in GRIP (1986-
509 1990) and DSS (2000-2009) ice cores. The solid lines (grey) refer to seasonal variations of the measurements for each year.
510 The black solid line indicates seasonal data of measurements in the year 1988. The dashed lines indicate the averaged seasonal
511 variations of measured [10]Be (black), [10]Be[P16spa] (blue), and [10]Be[LP67] (red) concentrations.

512   Firstly, there is no consistent seasonal cycle in the GRIP [10]Be measurement, indicating a strong role of local

513 meteorology. The model does not reproduce the mean seasonal cycle partly because the model was not run for the

514 exact same period. However, we note that the measurements for the year 1988 show an annual cycle similar to

515 that in the model, suggesting that the model [10]Be seasonality falls within the range of the observations. For the

516 DSS site, the model simulates the austral winter minima but not the austral fall maxima (February-April). These

517 model biases could be due to the limited model resolution and local effects (e.g., ice redistribution due to wind

518 blow) that are not resolved by the model. Such discrepancies were also reported by previous model studies using

519 the ECHAM5-HAM general circulation model (2.8° × 2.8°) over the overlap period (Heikkilä et al., 2008c; Pedro

520   et al., 2011b). Global model simulations at higher resolutions or using a regional model could help improve the

521   agreements between model results and measurements at Greenland and Antarctica. However, it should be kept in

522   mind that local surface processes can cause a high degree of spatial variability in the impurity concentrations in

523   ice cores even on short distances (Gfeller et al., 2014), which cannot be resolved in climate models.

524

525   **3.7 ^{10}Be/^{7}Be ratio**

526   Figure 10 shows the modeled zonal mean ^{10}Be$_{P16spa}$/^{7}Be$_{P16spa}$ ratios during boreal spring (March-May) and

527   austral spring (September-November), respectively, when the stratosphere-troposphere exchange is strong in

528   either of the two hemispheres. Also shown are the comparison of the altitudinal profile of the ^{10}Be$_{P16spa}$/^{7}Be$_{P16spa}$

529   ratio with measurements from three aircraft missions (Jordan et al., 2003). The model ^{10}Be$_{P16spa}$/^{7}Be$_{P16spa}$ ratio

530   generally lies within the ranges of measurements (Fig. 10c). Due to the decay of ^{7}Be and long residence time in

531   the stratosphere, the ^{10}Be/^{7}Be ratio is higher (>1.5) in the stratosphere and increase over the altitude, with a

532   maximum (>10) in the tropical stratosphere. During the period without strong stratospheric intrusion (e.g., autumn

533   season in Northern Hemisphere, Fig.10b), the monthly ^{10}Be/^{7}Be ratio near the surface is around 0.9~1. This

534   surface ^{10}Be/^{7}Be ratio could be up to 1.4 when the strong stratosphere-troposphere exchange happens (e.g., spring

535   season in Northern Hemisphere, Fig. 10a).
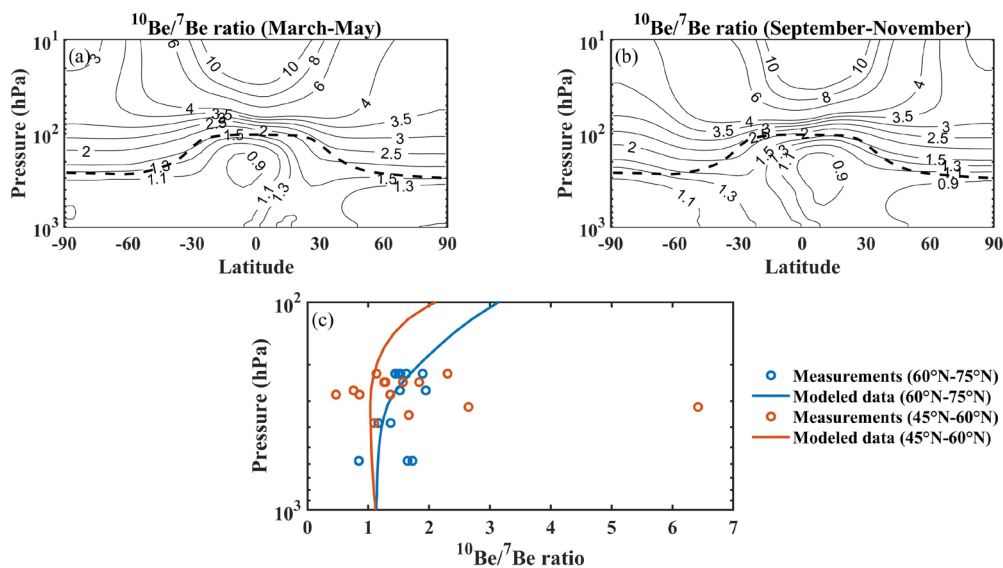
536
537   **Figure 10**. Upper panels: simulated ^{10}Be$_{P16spa}$/^{7}Be$_{P16spa}$ ratio in spring (March-May) (a) and autumn (September-November)
538   (b) averaged over the years 2008-2018. Lower panel (c): comparison between the annual averaged model ^{10}Be$_{P16spa}$/^{7}Be$_{P16spa}$
539   ratios (lines) and those from measurements (circles; Jordan et al., 2003). The comparison is shown for the latitude bands of
540   60°N-75°N and 45°N-60°N, respectively.

541   Figure 11 compares model surface air ^{7}Be$_{P16spa}$ and ^{10}Be$_{P16spa}$ concentrations and ^{10}Be$_{P16spa}$/^{7}Be$_{P16spa}$ ratios

542   with monthly mean observations in Tokyo (Yamagata et al., 2019) during the period of 2008-2014. Here we

543   mainly focus on the relative variations, and ^{7}Be and ^{10}Be data are normalized. The model captures the observed

544   variability in Tokyo well. The ^{7}Be and ^{10}Be show a peak in early spring (March-May) while the ^{10}Be/^{7}Be ratio

545   shows a wider peak over March-July. The summer minima of ^{7}Be and ^{10}Be are due to strong scavenging associated

546   with the monsoon/typhoon season precipitation. While the ^{10}Be/^{7}Be ratio is independent of precipitation

547   scavenging, the peaks of ^{10}Be/^{7}Be coincide well with the enhancements of stratospheric contribution in the model.

This indicates that the $^{10}Be/^{7}Be$ ratio is a better indicator of the vertical transport and stratospheric intrusion influences than either tracer alone.
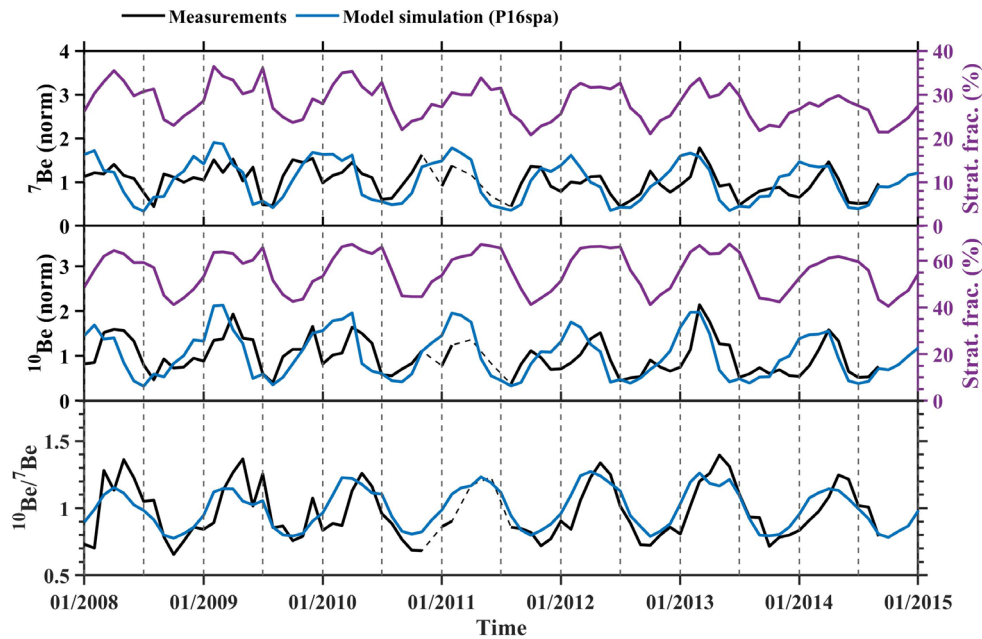
Figure 11. Comparison of monthly mean ^{7}Be (top panel), ^{10}Be (middle panel) concentrations, and $^{10}Be/^{7}Be$ ratio (bottom panel) between model results with P16spa production and measurements for the Tokyo station over the period 2008-2014. Noted that all ^{7}Be and ^{10}Be values are normalized to focus on variability. The dashed black line bridges the gap in measurements.

3.8 Solar modulation influences

Here we examine the ability of model to simulate the inter-annual variability of ^{7}Be surface air concentrations, especially whether the model can simulate the solar modulation influence using the updated production model. Figure 12 shows the comparison of model simulated annual mean surface air ^{7}Be concentrations with measurements during 2008-2018 from four sites: Kiruna, Ljungbyhed, Vienna and Hong Kong (Kong et al., 2022; Zheng et al., 2021a). The tropospheric ^{7}Be production rate from each site is also plotted for comparison as measured annual mean surface air ^{7}Be concentrations are predominantly influenced by the local tropospheric ^{7}Be production signal (Zheng et al., 2021a).

The model $^{7}Be_{P16spa}$ surface air concentrations show a better agreement with annual ^{7}Be measurements (higher R-value) compared to $^{7}Be_{LP67}$ concentrations at all surface sites (Fig. 12). The variability in the measurements (Kiruna, Ljungbyhed, and Vienna) agrees well with the trend in production, suggesting a dominant influence of solar modulations during this period. This is further supported by strong deviations between $^{7}Be_{P16spa}$ and $^{7}Be_{LP67}$ as no solar influence is considered in $^{7}Be_{LP67}$. This also emphasizes the importance of including solar modulation of the ^{7}Be and ^{10}Be production in modeling studies, especially for high-latitude regions. The mismatch of measurements and production at Kiruna from 2012 to 2015, together with the similar year-to-year variability between $^{7}Be_{P16spa}$ and $^{7}Be_{LP67}$, suggests the meteorological influence is dominant at Kiruna for this period. This also suggests that meteorological influences can suppress the solar signal in the ^{7}Be and ^{10}Be observations.

572
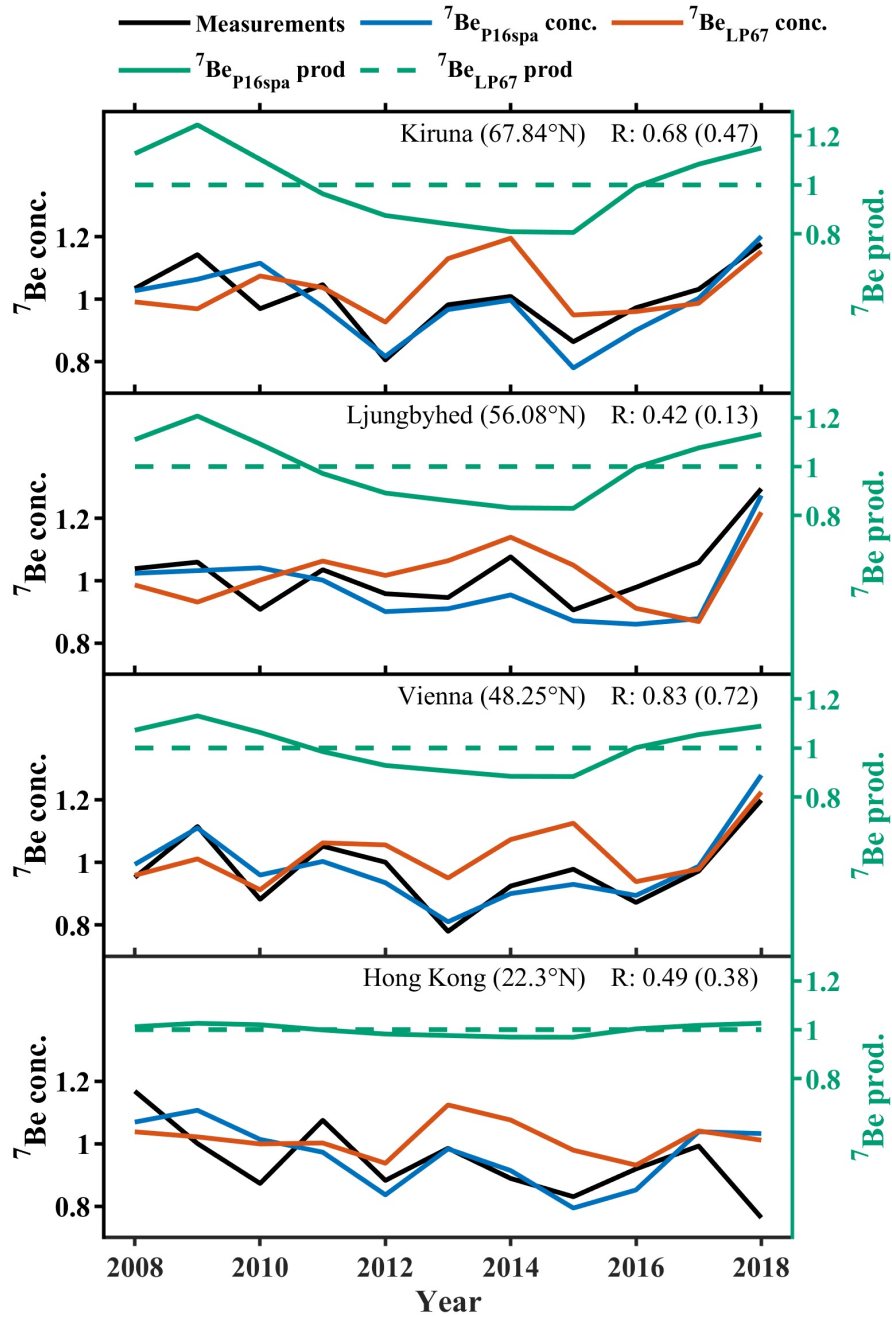
Figure 12. Comparison of annual mean model surface air ^{7}Be concentrations with measurements from 2008-2018. Also shown
are the model tropospheric ^{7}Be production (green lines) at each station. All data are normalized by being divided by the mean
over the first five years. The linear spearman correlation coefficient R-value is between ^{7}Be$_{P16spa}$ and measurements while the
value in the bracket is between ^{7}Be$_{LP67}$ and measurements.

4 Summary and conclusions

We have incorporated the ^{7}Be and ^{10}Be production rates derived from the CRAC:Be model considering realistic

spatial geomagnetic cut-off rigidities (P16spa) into the GEOS-Chem global chemical transport model, enabling

the model output to be quantitatively comparable with the measurements. In addition to the standard simulation

using P16spa production rate, we further conducted two sensitivity simulations: one with the default production

rate in GEOS-Chem based on an empirical approach (LP67), and one with production rate from the CRAC:Be but

considering only geomagnetic cut-off rigidities for a geocentric axial dipole (P16). On global average, the LP67 production rate is 60% higher compared to those of P16 and P16spa. The P16 production rate shows some regional differences (up to 50%) compared to the P16spa production rate.

In comparison with a large amount of air and deposition flux measurements, the model ^{7}Be$_{P16spa}$ shows good agreements with respect to surface air concentrations (93.7% of data within a factor of 2) and reasonably good agreements regarding deposition fluxes (60.9% of data within a factor of 2). The model simulates well the surface air concentration peaks in the subtropics associated strong downward transport from the stratosphere. This agreement is better than those using the default production ^{7}Be$_{LP16}$ and the ^{7}Be$_{P16}$ production with simplified axis symmetric dipole cut-off rigidity. The ^{7}Be$_{LP67}$ simulation overestimates the absolute value of ^{7}Be. The ^{7}Be$_{P16}$ simulation tends to produce a positive bias (~18%) for the ^{7}Be deposition fluxes in East Asia region, nevertheless, no large bias is found for ^{7}Be surface air concentrations. The surface deposition fluxes are more sensitive to the production in the mid- and upper-troposphere and downward transport of ^{7}Be from the stratosphere, due to the effect of precipitation scavenging throughout the troposphere.

For the first time, the ability of GEOS-Chem to simulate ^{10}Be is assessed with measurements. The model ^{10}Be$_{P16spa}$ results agree well with ^{10}Be observational data that were evaluated for dust influences or from the regions less influenced by dust (e.g., polar regions), while underestimating most samples that were not corrected for dust influences. This highlights the importance of examining the dust contribution to ^{10}Be measurements when using these data to evaluate models.

Independent of the production models, surface ^{7}Be and ^{10}Be concentrations from all three simulations show similar seasonal variations, suggesting a dominant meteorological influence. The model generally simulates well the annual cycle of ^{7}Be surface air concentrations and deposition fluxes at most sites in terms of amplitude and seasonality. The model fails to capture the "summer peak" in a few sites likely due to errors in convective transport during summer.

The model ^{10}Be/^{7}Be ratios also lie within the measurements, suggesting the stratosphere-troposphere exchange process is reasonably represented in the model. The mismatch of the peaks between ^{7}Be(^{10}Be) and ^{10}Be/^{7}Be ratios at the Tokyo site suggests that the ^{10}Be/^{7}Be ratio is a better indicator of the vertical transport and stratospheric influences than either tracer alone as the ratio is independent of precipitation scavenging.

Finally, we demonstrate the value and importance of including time-varying solar modulation in ^{7}Be and ^{10}Be production rates for model simulations of both tracers. It significantly improves the agreement of interannual variations between the model and measurements, especially at those surface sites from mid- and high- latitudes. The mismatch of trends in modeled ^{7}Be production rate and observed air concentrations at Kiruna from 2012-2015 also suggests that the solar signal can be suppressed by meteorological influences.

In summary, we have shown that with the state-of-the-art P16spa production rate, the ability of GEOS-Chem to reproduce the ^{7}Be and ^{10}Be measurements (including interannual variability of ^{7}Be) is significantly improved. While uncertainties in transport and deposition processes play a major role in the model performance, reduced uncertainties in the production rates, as demonstrated in this study, allow us to use ^{7}Be and ^{10}Be tracers as better tools for evaluating and testing transport and scavenging in global models. We recommend using the P16spa (versus default LP67) production rate for GEOS-Chem simulations of ^{7}Be and ^{10}Be in the future.

Author contributions. MZ initiated the study. MZ performed the analysis and interpretation with contributions from HL and FA. MZ conducted the GEOS-Chem model simulations with the help from MW and ZL. All authors discussed the results and edited the manuscript.

Competing interests. The authors declare that there is no conflict of interest.

Data and Code availability. Observational data for model validation are available in the references described in section 2.3. The two compiled ^{10}Be observation datasets are available in the Supplementary Information. The GEOS-Chem v14.0.2 model code, GEOS-Chem model output and ^{7}Be and ^{10}Be production rates are available at Zenodo repository (https://doi.org/10.5281/zenodo.8372652; Zheng et al., 2023a).

Acknowledgments. This project is supported by the Swedish Research Council (Dnr: 2021-06649) and the Swedish government funded Strategic Research Area: ModElling the Regional and Global Earth system, MERGE (MERGE). H. Liu acknowledges funding support from the NASA Modeling, Analysis and Prediction (MAP) program (grant 80NSSC17K0221) and Atmospheric Composition Campaign Data Analysis and Modeling program (grants NNX14AR07G and 80NSSC21K1455). F. Adolphi acknowledges support from the Helmholtz association (Grant number VH-NG 1501). R. Muscheler acknowledges support from the Swedish Research Council (grants DNR2013-8421 and DNR2018-05469). Z. Lu acknowledges Swedish Research Council Vetenskapsrådet (Grant No. 2022-03617). M. Wu acknowledges the National Natural Science Foundation of China (42111530184, 41901266). N. Prisle acknowledges the funding from the Academy of Finland (Grant Nos. 308238, 314175, and 335649). This project has received funding from the European Research Council (ERC) under the European Union's Horizon 2020 research and innovation programme, Project SURFACE (Grant Agreement No. 717022). The GEOS-Chem model is managed by the Atmospheric Chemistry Modeling Group at Harvard University. GEOS-Chem support team at Harvard University and Washington University in St. Louis (WashU) is acknowledged for their effort. GEOS-Chem input files were obtained from the GEOS-Chem Data Portal enabled by WashU.

References

Ajtic, J., Brattich, E., Sarvan, D., Djurdjevic, V., and Hernandez-Ceballos, M. A.: Factors affecting the ^{7}Be surface concentration and its extremely high occurrences over the Scandinavian Peninsula during autumn and winter, Chemosphere, 199, 278-285, https://doi.org/10.1016/j.chemosphere.2018.02.052, 2018.

Ajtić, J., Zorko, B., Nečemer, M., Sarvan, D., Rajačić, M., Krneta Nikolić, J., Todorović, D., Djurdjevic, V., Vodenik, B., Glavič Cindro, D., and Kožar Logar, J.: Characteristics of radioactivity in the surface air along the 45°N zonal belt in South-Eastern Europe, International Journal of Environmental Science and Technology, https://doi.org/10.1007/s13762-021-03814-0, 2021.

Aldahan, A., Possnert, G., and Vintersved, I.: Atmospheric interactions at northern high latitudes from weekly Be-isotopes in surface air, Applied Radiation and Isotopes, 54, 345-353, https://doi.org/10.1016/S0969-8043(00)00163-9, 2001.

Aldahan, A., Hedfors, J., Possnert, G., Kulan, A., Berggren, A. M., and Söderström, C.: Atmospheric impact on beryllium isotopes as solar activity proxy, Geophys Res Lett, 35, https://doi.org/10.1029/2008gl035189, 2008.

Aldahan, A., Possnert, G., Johnsen, S. J., Clausen, H. B., Isaksson, E., Karlen, W., and Hansson, M.: Sixty year ^{10}Be record from Greenland and Antarctica, Earth and Planetary Sciences, 107, 139-147, https://doi.org/10.1007/BF02840464, 1998.

Auer, M., Wagenbach, D., Wild, E. M., Wallner, A., Priller, A., Miller, H., Schlosser, C., and Kutschera, W.: Cosmogenic ^{26}Al in the atmosphere and the prospect of a ^{26}Al/^{10}Be chronometer to date old ice, Earth and Planetary Science Letters, 287, 453-462, https://doi.org/10.1016/j.epsl.2009.08.030, 2009.

Baroni, M., Bard, E., Petit, J.-R., Magand, O., and Bourlès, D.: Volcanic and solar activity, and atmospheric circulation influences on cosmogenic ^{10}Be fallout at Vostok and Concordia (Antarctica) over the last 60 years, Geochimica et Cosmochimica Acta, 75, 7132-7145, https://doi.org/10.1016/j.gca.2011.09.002, 2011.

Beer, J., McCracken, K., and Von Steiger, R.: Cosmogenic Radionuclides: Theory and Applications in the Terrestrial and Space Environments, Springer Berlin, Heidelberg, 428 pp., https://doi.org/10.1007/978-3-642-14651-0, 2012.

Berggren, A. M., Beer, J., Possnert, G., Aldahan, A., Kubik, P., Christl, M., Johnsen, S. J., Abreu, J., and Vinther, B. M.: A 600-year annual ^{10}Be record from the NGRIP ice core, Greenland, Geophys Res Lett, 36, L11801, https://doi.org/10.1029/2009gl038004, 2009.

Bey, I., Jacob, D. J., Yantosca, R. M., Logan, J. A., Field, B. D., Fiore, A. M., Li, Q., Liu, H. Y., Mickley, L. J., and Schultz, M. G.: Global modeling of tropospheric chemistry with assimilated meteorology: Model description and evaluation, Journal of Geophysical Research: Atmospheres, 106, 23073-23095, https://doi.org/10.1029/2001JD000807, 2001.

Bleichrodt, J. F.: Mean tropospheric residence time of cosmic-ray-produced beryllium 7 at north temperate latitudes, Journal of Geophysical Research: Oceans, 83, 3058-3062, https://doi.org/10.1029/JC083iC06p03058, 1978.

Brattich, E., Liu, H., Tositti, L., Considine, D. B., and Crawford, J. H.: Processes controlling the seasonal variations in ^{210}Pb and ^{7}Be at the Mt. Cimone WMO-GAW global station, Italy: a model analysis, Atmospheric Chemistry and Physics, 17, 1061-1080, https://doi.org/10.5194/acp-17-1061-2017, 2017.

Brattich, E., Liu, H., Zhang, B., Hernández-Ceballos, M. Á., Paatero, J., Sarvan, D., Djurdjevic, V., Tositti, L., and Ajtić, J.: Observation and modeling of high-7Be events in Northern Europe associated with the instability of the Arctic polar vortex in early 2003, Atmos. Chem. Phys. Discuss., 2021, 1-43, https://doi.org/10.5194/acp-2020-1121, 2021.

Burakowska, A., Kubicki, M., Myslek-Laurikainen, B., Piotrowski, M., Trzaskowska, H., and Sosnowiec, R.: Concentration of ^{7}Be, ^{210}Pb, ^{40}K, ^{137}Cs, ^{134}Cs radionuclides in the ground layer of the atmosphere in the polar (Hornsund, Spitsbergen) and mid-latitudes (Otwock-Swider, Poland) regions, J Environ Radioact, 240, 106739, https://doi.org/10.1016/j.jenvrad.2021.106739, 2021.

696   Chabrillat, S., Vigouroux, C., Christophe, Y., Engel, A., Errera, Q., Minganti, D., Monge-Sanz, B. M., Segers, A.,

697   and Mahieu, E.: Comparison of mean age of air in five reanalyses using the BASCOE transport model,

698   Atmospheric Chemistry and Physics, 18, 14715-14735, https://doi.org/10.5194/acp-18-14715-2018, 2018.

699   Chae, J.-S. and Kim, G.: Large seasonal variations in fine aerosol precipitation rates revealed using cosmogenic

700   ^{7}Be as a tracer, Science of The Total Environment, 673, 1-6, https://doi.org/10.1016/j.scitotenv.2019.03.482,

701   2019.

702   Chang, J. C. and Hanna, S. R.: Air quality model performance evaluation, Meteorology and Atmospheric Physics,

703   87, https://doi.org/10.1007/s00703-003-0070-7, 2004.

704   Chmeleff, J., von Blanckenburg, F., Kossert, K., and Jakob, D.: Determination of the ^{10}Be half-life by

705   multicollector ICP-MS and liquid scintillation counting, Nuclear Instruments and Methods in Physics Research

706   Section   B: Beam   Interactions   with   Materials   and   Atoms,   268,   192-199,

707   https://doi.org/10.1016/j.nimb.2009.09.012, 2010.

708   Copeland, K.: CARI-7 Documentation: Geomagnetic Cutoff Rigidity Calculations and Tables for 1965-2010,

709   United States. Department of Transportation. Federal Aviation Administration, 2018.

710   Courtier, J., Sdraulig, S., and Hirth, G.: ^{7}Be and ^{210}Pb wet/dry deposition in Melbourne, Australia and the

711   development of deployable units for radiological emergency monitoring, Journal of Environmental Radioactivity,

712   178-179, 419-425, https://doi.org/10.1016/j.jenvrad.2017.07.004, 2017.

713   Delaygue, G., Bekki, S., and Bard, E.: Modelling the stratospheric budget of beryllium isotopes, Tellus B:

714   Chemical and Physical Meteorology, 67, 28582, https://doi.org/10.3402/tellusb.v67.28582, 2015.

715   Dibb, J. E., Talbot, R. W., and Gregory, G. L.: Beryllium 7 and Lead 210 in the western hemisphere Arctic

716   atmosphere: Observations from three recent aircraft-based sampling programs, Journal of Geophysical Research:

717   Atmospheres, 97, 16709-16715, https://doi.org/10.1029/91JD01807, 1992.

718   Dibb, J. E., Meeker, L. D., Finkel, R. C., Southon, J. R., Caffee, M. W., and Barrie, L. A.: Estimation of

719   stratospheric input to the Arctic troposphere: ^{7}Be and ^{10}Be in aerosols at Alert, Canada, 99, 12855-12864,

720   https://doi.org/10.1029/94jd00742, 1994.

721   Du, J., Du, J., Baskaran, M., Bi, Q., Huang, D., and Jiang, Y.: Temporal variations of atmospheric depositional

722   fluxes of ^{7}Be and ^{210}Pb over 8 years (2006-2013) at Shanghai, China, and synthesis of global fallout data, Journal

723   of Geophysical Research: Atmospheres, 120, 4323-4339, https://doi.org/10.1002/2014jd022807, 2015.

724   Dueñas, C., Gordo, E., Liger, E., Cabello, M., Cañete, S., Pérez, M., and Torre-Luque, P. d. l.: ^{7}Be, ^{210}Pb and ^{40}K

725   depositions over 11 years in Málaga, Journal of Environmental Radioactivity, 178-179, 325-334,

726   https://doi.org/10.1016/j.jenvrad.2017.09.010, 2017.

727   Dutkiewicz, V. A. and Husain, L.: Stratospheric and tropospheric components of ^{7}Be in surface air, Journal of

728   Geophysical Research: Atmospheres, 90, 5783-5788, https://doi.org/10.1029/JD090iD03p05783, 1985.

729   Eastham, S. D., Weisenstein, D. K., and Barrett, S. R. H.: Development and evaluation of the unified tropospheric–

730   stratospheric chemistry extension (UCX) for the global chemistry-transport model GEOS-Chem, Atmospheric

731   Environment, 89, 52-63, https://doi.org/10.1016/j.atmosenv.2014.02.001, 2014.

732   Elsässer, C.: Exploration of ^{10}Be ice core records using a climatological model approach: Cosmogenic production

733   versus climate variability, https://doi.org/10.11588/heidok.00016349, 2013.

734 Elsässer, C., Wagenbach, D., Weller, R., Auer, M., Wallner, A., and Christl, M.: Continuous 25-yr aerosol records

735 at coastal Antarctica, Tellus B: Chemical and Physical Meteorology, 63, 920-934, https://doi.org/10.1111/j.1600-

736 0889.2011.00543.x, 2011.

737 Field, C. V., Schmidt, G. A., Koch, D., and Salyk, C.: Modeling production and climate-related impacts on ^{10}Be

738 concentration in ice cores, Journal of Geophysical Research, 111, https://doi.org/10.1029/2005jd006410, 2006.

739 Gao, J., Korte, M., Panovska, S., Rong, Z., and Wei, Y.: Effects of the Laschamps Excursion on Geomagnetic

740 Cutoff Rigidities, Geochemistry, Geophysics, Geosystems, 23, e2021GC010261,

741 https://doi.org/10.1029/2021GC010261, 2022.

742 Gelaro, R., McCarty, W., Suarez, M. J., Todling, R., Molod, A., Takacs, L., Randles, C., Darmenov, A.,

743 Bosilovich, M. G., Reichle, R., Wargan, K., Coy, L., Cullather, R., Draper, C., Akella, S., Buchard, V., Conaty,

744 A., da Silva, A., Gu, W., Kim, G. K., Koster, R., Lucchesi, R., Merkova, D., Nielsen, J. E., Partyka, G., Pawson,

745 S., Putman, W., Rienecker, M., Schubert, S. D., Sienkiewicz, M., and Zhao, B.: The Modern-Era Retrospective

746 Analysis for Research and Applications, Version 2 (MERRA-2), J Clim, Volume 30, 5419-5454, 10.1175/JCLI-

747 D-16-0758.1, 2017a.

748 Gelaro, R., McCarty, W., Suárez, M. J., Todling, R., Molod, A., Takacs, L., Randles, C. A., Darmenov, A.,

749 Bosilovich, M. G., Reichle, R., Wargan, K., Coy, L., Cullather, R., Draper, C., Akella, S., Buchard, V., Conaty,

750 A., da Silva, A. M., Gu, W., Kim, G.-K., Koster, R., Lucchesi, R., Merkova, D., Nielsen, J. E., Partyka, G.,

751 Pawson, S., Putman, W., Rienecker, M., Schubert, S. D., Sienkiewicz, M., and Zhao, B.: The Modern-Era

752 Retrospective Analysis for Research and Applications, Version 2 (MERRA-2), Journal of Climate, 30, 5419-5454,

753 https://doi.org/10.1175/JCLI-D-16-0758.1, 2017b.

754 Gfeller, G., Fischer, H., Bigler, M., Schüpbach, S., Leuenberger, D., and Mini, O.: Representativeness and

755 seasonality of major ion records derived from NEEM firn cores, The Cryosphere, 8, 1855-1870,

756 https://doi.org/10.5194/tc-8-1855-2014, 2014.

757 Golubenko, K., Rozanov, E., Kovaltsov, G., and Usoskin, I.: Zonal Mean Distribution of Cosmogenic Isotope

758 (^{7}Be, ^{10}Be, ^{14}C, and ^{36}Cl) Production in Stratosphere and Troposphere, Journal of Geophysical Research:

759 Atmospheres, 127, e2022JD036726, https://doi.org/10.1029/2022JD036726, 2022.

760 Golubenko, K., Rozanov, E., Kovaltsov, G., Leppänen, A.-P., Sukhodolov, T., and Usoskin, I.: Application of

761 CCM SOCOL-AERv2-BE to cosmogenic beryllium isotopes: description and validation for polar regions,

762 Geoscientific Model Development, 14, 7605-7620, https://doi.org/10.5194/gmd-14-7605-2021, 2021.

763 Graham, I., Ditchburn, R., and Barry, B.: Atmospheric deposition of ^{7}Be and ^{10}Be in New Zealand rain (1996-

764 98), Geochimica et Cosmochimica Acta, 67, 361-373, https://doi.org/10.1016/S0016-7037(02)01092-X, 2003.

765 Heikkilä, U. and Smith, A. M.: Influence of model resolution on the atmospheric transport of ^{10}Be, Atmospheric

766 Chemistry and Physics, 12, 10601-10612, https://doi.org/10.5194/acp-12-10601-2012, 2012.

767 Heikkilä, U. and Smith, A. M.: Production rate and climate influences on the variability of ^{10}Be deposition

768 simulated by ECHAM5-HAM: Globally, in Greenland, and in Antarctica, Journal of Geophysical Research:

769 Atmospheres, 118, 2506-2520, https://doi.org/10.1002/jgrd.50217, 2013.

770 Heikkilä, U., Beer, J., and Alfimov, V.: Beryllium-10 and beryllium-7 in precipitation in Dübendorf (440 m) and

771 at Jungfraujoch (3580 m), Switzerland (1998–2005), Journal of Geophysical Research, 113, D11104,

772 https://doi.org/10.1029/2007jd009160, 2008a.

773   Heikkilä, U., Beer, J., and Feichter, J.: Modeling cosmogenic radionuclides ^{10}Be and ^{7}Be during the Maunder
774   Minimum using the ECHAM5-HAM General Circulation Model, Atmospheric Chemistry and Physics, 8, 2797-
775   2809, https://doi.org/10.5194/acp-8-2797-2008, 2008b.

776   Heikkilä, U., Beer, J., and Feichter, J.: Meridional transport and deposition of atmospheric ^{10}Be, Atmospheric
777   Chemistry and Physics, 9, 515-527, https://doi.org/10.5194/acp-9-515-2009, 2009.

778   Heikkilä, U., Beer, J., Abreu, J. A., and Steinhilber, F.: On the Atmospheric Transport and Deposition of the
779   Cosmogenic Radionuclides (^{10}Be): A Review, Space Science Reviews, 176, 321-332,
780   https://doi.org/10.1007/s11214-011-9838-0, 2013.

781   Heikkilä, U., Beer, J., Jouzel, J., Feichter, J., and Kubik, P.: ^{10}Be measured in a GRIP snow pit and modeled using
782   the ECHAM5-HAM general circulation model, Geophys Res Lett, 35, https://doi.org/10.1029/2007gl033067,
783   2008c.

784   Herbst, K., Muscheler, R., and Heber, B.: The new local interstellar spectra and their influence on the production
785   rates of the cosmogenic radionuclides ^{10}Be and ^{14}C, Journal of Geophysical Research: Space Physics, 122, 23-34,
786   https://doi.org/10.1002/2016ja023207, 2017.

787   Hernandez-Ceballos, M. A., Cinelli, G., Ferrer, M. M., Tollefsen, T., De Felice, L., Nweke, E., Tognoli, P. V.,
788   Vanzo, S., and De Cort, M.: A climatology of ^{7}Be in surface air in European Union, J Environ Radioact, 141, 62-
789   70, https://doi.org/10.1016/j.jenvrad.2014.12.003, 2015.

790   Hernández-Ceballos, M. A., Brattich, E., and Ajtić, J.: Airflow and teleconnection patterns driving the spatial and
791   temporal variability of high ^{7}Be air concentrations in Europe, Chemosphere, 303, 135194,
792   https://doi.org/10.1016/j.chemosphere.2022.135194, 2022.

793   Hernández-Ceballos, M. A., Brattich, E., Cinelli, G., Ajtić, J., and Djurdjevic, V.: Seasonality of ^{7}Be
794   concentrations in Europe and influence of tropopause height, Tellus B: Chemical and Physical Meteorology, 68,
795   29534, https://doi.org/10.3402/tellusb.v68.29534, 2016.

796   Hu, J., Sha, Z., Wang, J., Du, J., and Ma, Y.: Atmospheric deposition of ^{7}Be, ^{210}Pb in Xining, a typical city on the
797   Qinghai-Tibet Plateau, China, Journal of Radioanalytical and Nuclear Chemistry, 324, 1141-1150,
798   https://doi.org/10.1007/s10967-020-07127-3, 2020.

799   Huang, J., Kang, S., Shen, C., Cong, Z., Liu, K., Wang, W., and Liu, L.: Concentration and seasonal variation of
800   10Be in surface aerosols of Lhasa, Tibet, Chinese Science Bulletin, 55, 2572-2578,
801   https://doi.org/10.1007/s11434-010-3233-1, 2010.

802   Huh, C.-A., Su, C.-C., and Shiau, L.-J.: Factors controlling temporal and spatial variations of atmospheric
803   deposition of ^{7}Be and ^{210}Pb in northern Taiwan, Journal of Geophysical Research, 111,
804   https://doi.org/10.1029/2006jd007180, 2006.

805   Ioannidou, A. and Papastefanou, C.: Precipitation scavenging of ^{7}Be and ^{137}Cs radionuclides in air, J Environ
806   Radioact, 85, 121-136, https://doi.org/10.1016/j.jenvrad.2005.06.005, 2006.

807   Jordan, C. E., Dibb, J. E., and Finkel, R. C.: ^{10}Be/^{7}Be tracer of atmospheric transport and stratosphere-troposphere
808   exchange, Journal of Geophysical Research: Atmospheres, 108, https://doi.org/10.1029/2002JD002395, 2003.

809   Koch, D. and Rind, D.: Beryllium 10/beryllium 7 as a tracer of stratospheric transport, Journal of Geophysical
810   Research: Atmospheres, 103, 3907-3917, https://doi.org/10.1029/97JD03117, 1998.

811 Koch, D. M., Jacob, D. J., and Graustein, W. C.: Vertical transport of tropospheric aerosols as indicated by [7]Be
812 and ^{210}Pb in a chemical tracer model, Journal of Geophysical Research: Atmospheres, 101, 18651-18666,
813 https://doi.org/10.1029/96JD01176, 1996.

814 Koldobskiy, S. A., Bindi, V., Corti, C., Kovaltsov, G. A., and Usoskin, I. G.: Validation of the Neutron Monitor
815 Yield Function Using Data From AMS-02 Experiment, 2011–2017, Journal of Geophysical Research: Space
816 Physics, 124, 2367-2379, https://doi.org/10.1029/2018ja026340, 2019.

817 Kong, Y. C., Lee, O. S. M., and Yung, C. H.: Study of the naturally occurring radionuclide Beryllium-7 (Be-7) in
818 Hong Kong, Journal of Environmental Radioactivity, 246, 106850,
819 https://doi.org/10.1016/j.jenvrad.2022.106850, 2022.

820 Kusmierczyk-Michulec, J., Gheddou, A., and Nikkinen, M.: Influence of precipitation on [7]Be concentrations in
821 air as measured by CTBTO global monitoring system, J Environ Radioact, 144, 140-151,
822 https://doi.org/10.1016/j.jenvrad.2015.03.014, 2015.

823 Lal, D. and Peters, B.: Cosmic Ray Produced Radioactivity on the Earth, in: Kosmische Strahlung II / Cosmic
824 Rays II, edited by: Sitte, K., Springer Berlin Heidelberg, Berlin, Heidelberg, 551-612,
825 https://doi.org/10.1007/978-3-642-46079-1_7, 1967.

826 Lee, H. I., Huh, C. A., Lee, T., and Huang, N. E.: Time series study of a 17-year record of [7]Be and ^{210}Pb fluxes in
827 northern Taiwan using ensemble empirical mode decomposition, J Environ Radioact, 147, 14-21,
828 https://doi.org/10.1016/j.jenvrad.2015.04.017, 2015.

829 Leppänen, A. P., Pacini, A. A., Usoskin, I. G., Aldahan, A., Echer, E., Evangelista, H., Klemola, S., Kovaltsov,
830 G. A., Mursula, K., and Possnert, G.: Cosmogenic [7]Be in air: A complex mixture of production and transport,
831 Journal of Atmospheric and Solar-Terrestrial Physics, 72, 1036-1043, https://doi.org/10.1016/j.jastp.2010.06.006,
832 2010.

833 Lin, J.-T. and McElroy, M. B.: Impacts of boundary layer mixing on pollutant vertical profiles in the lower
834 troposphere: Implications to satellite remote sensing, Atmospheric Environment, 44, 1726-1739,
835 https://doi.org/10.1016/j.atmosenv.2010.02.009, 2010.

836 Lin, S.-J. and Rood, R. B.: Multidimensional Flux-Form Semi-Lagrangian Transport Schemes, Monthly Weather
837 Review, 124, 2046-2070, https://doi.org/10.1175/1520-0493(1996)124<2046:MFFSLT>2.0.CO;2, 1996.

838 Liu, H., Jacob, D. J., Bey, I., and Yantosca, R. M.: Constraints from ^{210}Pb and [7]Be on wet deposition and transport
839 in a global three-dimensional chemical tracer model driven by assimilated meteorological fields, Journal of
840 Geophysical Research: Atmospheres, 106, 12109-12128, https://doi.org/10.1029/2000jd900839, 2001.

841 Liu, H., Jacob, D. J., Dibb, J. E., Fiore, A. M., and Yantosca, R. M.: Constraints on the sources of tropospheric
842 ozone from [210]Pb-[7]Be-O_3 correlations, Journal of Geophysical Research: Atmospheres, 109,
843 https://doi.org/10.1029/2003JD003988, 2004.

844 Liu, H., Considine, D. B., Horowitz, L. W., Crawford, J. H., Rodriguez, J. M., Strahan, S. E., Damon, M. R.,
845 Steenrod, S. D., Xu, X., Kouatchou, J., Carouge, C., and Yantosca, R. M.: Using beryllium-7 to assess cross-
846 tropopause transport in global models, Atmospheric Chemistry and Physics, 16, 4641-4659,
847 https://doi.org/10.5194/acp-16-4641-2016, 2016.

848 Liu, X., Fu, Y., Bi, Y., Zhang, L., Zhao, G., Xian, F., and Zhou, W.: Monitoring Surface [10]Be/[7]Be Directly Reveals
849 Stratospheric Air Intrusion in Sichuan Basin, China, Journal of Geophysical Research: Atmospheres, 127,
850 e2022JD036543, https://doi.org/10.1029/2022JD036543, 2022a.

851   Liu, X., Fu, Y., Wang, Q., Bi, Y., Zhang, L., Zhao, G., Xian, F., Cheng, P., Zhang, L., Zhou, J., and Zhou, W.:
852   Unraveling the process of aerosols secondary formation and removal based on cosmogenic beryllium-7 and
853   beryllium-10, Science of The Total Environment, 821, 153293, https://doi.org/10.1016/j.scitotenv.2022.153293,
854   2022b.

855   Maejima, Y., Matsuzaki, H., and Higashi, T.: Application of cosmogenic ^{10}Be to dating soils on the raised coral
856   reef terraces of Kikai Island, southwest Japan, Geoderma, 126, 389-399,
857   https://doi.org/10.1016/j.geoderma.2004.10.004, 2005.

858   Mari, C., Jacob, D. J., and Bechtold, P.: Transport and scavenging of soluble gases in a deep convective cloud,
859   Journal of Geophysical Research: Atmospheres, 105, 22255-22267, https://doi.org/10.1029/2000JD900211,
860   2000.

861   Masarik, J. and Beer, J.: Simulation of particle fluxes and cosmogenic nuclide production in the Earth's
862   atmosphere, Journal of Geophysical Research: Atmospheres, 104, 12099-12111,
863   https://doi.org/10.1029/1998jd200091, 1999.

864   Masarik, J. and Beer, J.: An updated simulation of particle fluxes and cosmogenic nuclide production in the Earth's
865   atmosphere, Journal of Geophysical Research, 114, https://doi.org/10.1029/2008jd010557, 2009.

866   Méndez-García, C. G., Rojas-López, G., Padilla, S., Solís, C., Chávez, E., Acosta, L., and Huerta, A.: The impact
867   of stable ^{27}Al in ^{26}Al/^{10}Be meteoric ratio in PM2.5 from an urban area, Journal of Environmental Radioactivity,
868   246, 106832, https://doi.org/10.1016/j.jenvrad.2022.106832, 2022.

869   Monaghan, M. C., Krishnaswami, S., and Turekian, K. K.: The global-average production rate of ^{10}Be, Earth and
870   Planetary Science Letters, 76, 279-287, https://doi.org/10.1016/0012-821X(86)90079-8, 1986.

871   Murray, L. T., Leibensperger, E. M., Orbe, C., Mickley, L. J., and Sulprizio, M.: GCAP 2.0: a global 3-D
872   chemical-transport model framework for past, present, and future climate scenarios, Geosci. Model Dev., 14,
873   5789-5823, 10.5194/gmd-14-5789-2021, 2021.

874   Muscheler, R., Joos, F., Beer, J., Müller, S. A., Vonmoos, M., and Snowball, I.: Solar activity during the last
875   1000yr inferred from radionuclide records, Quaternary Science Reviews, 26, 82-97,
876   https://doi.org/10.1016/j.quascirev.2006.07.012, 2007.

877   Myers, J. L., Well, A. D., and Lorch Jr, R. F.: Research design and statistical analysis, Routledge2013.

878   Nevalainen, J., Usoskin, I. G., and Mishev, A.: Eccentric dipole approximation of the geomagnetic field:
879   Application to cosmic ray computations, Advances in Space Research, 52, 22-29,
880   https://doi.org/10.1016/j.asr.2013.02.020, 2013.

881   Pacini, A. A., Usoskin, I. G., Mursula, K., Echer, E., and Evangelista, H.: Signature of a sudden stratospheric
882   warming in the near-ground ^{7}Be flux, Atmospheric Environment, 113, 27-31,
883   https://doi.org/10.1016/j.atmosenv.2015.04.065, 2015.

884   Padilla, S., Lopez-Gutierrez, J. M., Manjon, G., Garcia-Tenorio, R., Galvan, J. A., and Garcia-Leon, M.: Meteoric
885   ^{10}Be in aerosol filters in the city of Seville, J Environ Radioact, 196, 15-21,
886   https://doi.org/10.1016/j.jenvrad.2018.10.009, 2019.

887   Pedro, J. B., Smith, A. M., Simon, K. J., van Ommen, T. D., and Curran, M. A. J.: High-resolution records of the
888   beryllium-10 solar activity proxy in ice from Law Dome, East Antarctica: measurement, reproducibility and
889   principal trends, Climate of the Past, 7, 707-721, https://doi.org/10.5194/cp-7-707-2011, 2011a.

890   Pedro, J. B., Heikkilä, U. E., Klekociuk, A., Smith, A. M., van Ommen, T. D., and Curran, M. A. J.: Beryllium-
891   10 transport to Antarctica: Results from seasonally resolved observations and modeling, Journal of Geophysical
892   Research: Atmospheres, 116, https://doi.org/10.1029/2011jd016530, 2011b.

893   Pedro, J. B., McConnell, J. R., van Ommen, T. D., Fink, D., Curran, M. A. J., Smith, A. M., Simon, K. J., Moy,
894   A. D., and Das, S. B.: Solar and climate influences on ice core ^{10}Be records from Antarctica and Greenland during
895   the neutron monitor era, Earth and Planetary Science Letters, 355-356, 174-186,
896   https://doi.org/10.1016/j.epsl.2012.08.038, 2012.

897   Pilchowski, J., Kopp, A., Herbst, K., and Heber, B.: On the definition and calculation of a generalised McIlwain
898   parameter, Astrophys. Space Sci. Trans., 6, 9-17, https://doi.org/10.5194/astra-6-9-2010, 2010.

899   Poluianov, S. V., Kovaltsov, G. A., Mishev, A. L., and Usoskin, I. G.: Production of cosmogenic isotopes ^{7}Be,
900   ^{10}Be,^{14}C, ^{22}Na, and ^{36}Cl in the atmosphere: Altitudinal profiles of yield functions, Journal of Geophysical
901   Research: Atmospheres, 121, 8125-8136, https://doi.org/10.1002/2016jd025034, 2016.

902   Raisbeck, G. M., Yiou, F., Fruneau, M., Loiseaux, J. M., Lieuvin, M., and Ravel, J. C.: Deposition rate and
903   seasonal variations in precipitation of cosmogenic ^{10}Be, Nature, 282, 279-280, https://doi.org/10.1038/282279a0,
904   1979.

905   Raisbeck, G. M., Yiou, F., Fruneau, M., Loiseaux, J. M., Lieuvin, M., and Ravel, J. C.: Cosmogenic ^{10}Be/^{7}Be as
906   a probe of atmospheric transport processes, Geophys Res Lett, 8, 1015-1018,
907   http://dx.doi.org/10.1029/GL008i009p01015, 1981.

908   Rodriguez-Perulero, A., Baeza, A., and Guillen, J.: Seasonal evolution of ^{7,10}Be and ^{22}Na in the near surface
909   atmosphere of Caceres (Spain), J Environ Radioact, 197, 55-61, https://doi.org/10.1016/j.jenvrad.2018.11.015,
910   2019.

911   Sangiorgi, M., Hernández Ceballos, M. A., Iurlaro, G., Cinelli, G., and de Cort, M.: 30 years of European
912   Commission Radioactivity Environmental Monitoring data bank (REMdb) – an open door to boost environmental
913   radioactivity research, Earth System Science Data, 11, 589-601, https://doi.org/10.5194/essd-11-589-2019, 2019.

914   Smart, D. F. and Shea, M. A.: A review of geomagnetic cutoff rigidities for earth-orbiting spacecraft, Advances
915   in Space Research, 36, 2012-2020, https://doi.org/10.1016/j.asr.2004.09.015, 2005.

916   Somayajulu, B. L. K., Sharma, P., Beer, J., Bonani, G., Hofmann, H. J., Morenzoni, E., Nessi, M., Suter, M., and
917   Wölfli, W.: ^{10}Be annual fallout in rains in India, Nuclear Instruments and Methods in Physics Research Section
918   B: Beam Interactions with Materials and Atoms, 5, 398-403, https://doi.org/10.1016/0168-583X(84)90549-4,
919   1984.

920   Spiegl, T. C., Yoden, S., Langematz, U., Sato, T., Chhin, R., Noda, S., Miyake, F., Kusano, K., Schaar, K., and
921   Kunze, M.: Modeling the Transport and Deposition of ^{10}Be Produced by the Strongest Solar Proton Event During
922   the Holocene, Journal of Geophysical Research: Atmospheres, 127, e2021JD035658,
923   https://doi.org/10.1029/2021JD035658, 2022.

924   Sukhodolov, T., Usoskin, I., Rozanov, E., Asvestari, E., Ball, W. T., Curran, M. A., Fischer, H., Kovaltsov, G.,
925   Miyake, F., Peter, T., Plummer, C., Schmutz, W., Severi, M., and Traversi, R.: Atmospheric impacts of the
926   strongest known solar particle storm of 775 AD, Sci Rep, 7, 45257, https://doi.org/10.1038/srep45257, 2017.

927   Terzi, L. and Kalinowski, M.: World-wide seasonal variation of ^{7}Be related to large-scale atmospheric circulation
928   dynamics, J Environ Radioact, 178-179, 1-15, https://doi.org/10.1016/j.jenvrad.2017.06.031, 2017.

929 Terzi, L., Kalinowski, M., Schoeppner, M., and Wotawa, G.: How to predict seasonal weather and monsoons with

930 radionuclide monitoring, Sci Rep, 9, 2729, https://doi.org/10.1038/s41598-019-39664-7, 2019.

931 Uhlar, R., Harokova, P., Alexa, P., and Kacmarik, M.: [7]Be atmospheric activity concentration and meteorological

932 data: Statistical analysis and two-layer atmospheric model, J Environ Radioact, 219, 106278,

933 https://doi.org/10.1016/j.jenvrad.2020.106278, 2020.

934 Usoskin, I. G., Field, C. V., Schmidt, G. A., Leppänen, A.-P., Aldahan, A., Kovaltsov, G. A., Possnert, G., and

935 Ungar, R. K.: Short-term production and synoptic influences on atmospheric [7]Be concentrations, Journal of

936 Geophysical Research, 114, D06108, https://doi.org/10.1029/2008jd011333, 2009.

937 Villarreal, R. E., Arazi, A., and Fernandez Niello, J. O.: Correlation between the latitudinal profile of the [7]Be air

938 concentration and the Hadley cell extent in the Southern Hemisphere, J Environ Radioact, 244-245, 106760,

939 https://doi.org/10.1016/j.jenvrad.2021.106760, 2022.

940 Wang, Q., Jacob, D. J., Fisher, J. A., Mao, J., Leibensperger, E. M., Carouge, C. C., Le Sager, P., Kondo, Y.,

941 Jimenez, J. L., Cubison, M. J., and Doherty, S. J.: Sources of carbonaceous aerosols and deposited black carbon

942 in the Arctic in winter-spring: implications for radiative forcing, Atmos. Chem. Phys., 11, 12453-12473,

943 https://doi.org/10.5194/acp-11-12453-2011, 2011.

944 Waugh, D. and Hall, T.: Age of Stratospheric Air: Theory, Observations, and Models, Reviews of Geophysics,

945 40, 1-1-1-26, https://doi.org/10.1029/2000rg000101, 2002.

946 Wesely, M. L.: Parameterization of surface resistances to gaseous dry deposition in regional-scale numerical

947 models, Atmospheric Environment, 23, 1293-1304, https://doi.org/10.1016/0004-6981(89)90153-4, 1989.

948 Wu, S., Mickley, L. J., Jacob, D. J., Logan, J. A., Yantosca, R. M., and Rind, D.: Why are there large differences

949 between models in global budgets of tropospheric ozone?, Journal of Geophysical Research: Atmospheres, 112,

950 https://doi.org/10.1029/2006JD007801, 2007.

951 Yamagata, T., Nagai, H., Matsuzaki, H., and Narasaki, Y.: Decadal variations of atmospheric [7]Be and [10]Be

952 concentrations between 1998 and 2014 in Japan, Nuclear Instruments and Methods in Physics Research Section

953 B: Beam Interactions with Materials and Atoms, 455, 265-270, https://doi.org/10.1016/j.nimb.2018.12.029, 2019.

954 Yu, K., Keller, C. A., Jacob, D. J., Molod, A. M., Eastham, S. D., and Long, M. S.: Errors and improvements in

955 the use of archived meteorological data for chemical transport modeling: an analysis using GEOS-Chem v11-01

956 driven by GEOS-5 meteorology, Geosci. Model Dev., 11, 305-319, https://doi.org/10.5194/gmd-11-305-2018,

957 2018.

958 Zhang, B., Liu, H., Crawford, J. H., Chen, G., Fairlie, T. D., Chambers, S., Kang, C. H., Williams, A. G., Zhang,

959 K., Considine, D. B., Sulprizio, M. P., and Yantosca, R. M.: Simulation of radon-222 with the GEOS-Chem global

960 model: emissions, seasonality, and convective transport, Atmos. Chem. Phys., 21, 1861-1887,

961 https://doi.org/10.5194/acp-21-1861-2021, 2021a.

962 Zhang, F., Wang, J., Baskaran, M., Zhong, Q., Wang, Y., Paatero, J., and Du, J.: A global dataset of atmospheric

963 [7]Be and ^{210}Pb measurements: annual air concentration and depositional flux, Earth System Science Data, 13, 2963-

964 2994, https://doi.org/10.5194/essd-13-2963-2021, 2021b.

965 Zheng, M., Liu, H., Adolphi, F., Muscheler, R., Lu, Z., Wu, M., and Prisle, N. L.: Simulations of [7]Be and [10]Be

966 with the GEOS-Chem global model v14.0.2 using state-of-the-art production rates, Zenodo,

967 https://doi.org/10.5281/zenodo.8372652, 2023a.

968   Zheng, M., Sjolte, J., Adolphi, F., Aldahan, A., Possnert, G., Wu, M., and Muscheler, R.: Solar and meteorological
969   influences on seasonal atmospheric ^{7}Be in Europe for 1975 to 2018, Chemosphere, 263,
970   https://doi.org/10.1016/j.chemosphere.2020.128318, 2021a.

971   Zheng, M., Adolphi, F., Sjolte, J., Aldahan, A., Possnert, G., Wu, M., Chen, P., and Muscheler, R.: Solar and
972   climate signals revealed by seasonal ^{10}Be data from the NEEM ice core project for the neutron monitor period,
973   Earth and Planetary Science Letters, 541, https://doi.org/10.1016/j.epsl.2020.116273, 2020.

974   Zheng, M., Adolphi, F., Sjolte, J., Aldahan, A., Possnert, G., Wu, M., Chen, P., and Muscheler, R.: Solar Activity
975   of the Past 100 Years Inferred From ^{10}Be in Ice Cores—Implications for Long-Term Solar Activity
976   Reconstructions, Geophys Res Lett, 48, e2020GL090896, https://doi.org/10.1029/2020GL090896, 2021b.

977   Zheng, M., Adolphi, F., Paleari, C., Tao, Q., Erhardt, T., Christl, M., Wu, M., Lu, Z., Hörhold, M., Chen, P., and
978   Muscheler, R.: Solar, Atmospheric, and Volcanic Impacts on 10Be Depositions in Greenland and Antarctica
979   During the Last 100 Years, Journal of Geophysical Research: Atmospheres, 128, e2022JD038392,
980   https://doi.org/10.1029/2022JD038392, 2023b.

981

982

983